In-situ speciation of arsenic contaminated soil using synchrotron based micro-spectroscopy

Markus Gräfe[a*], Matthew A. Marcus[b], and Donald L. Sparks[a]

[a]Molecular Environmental Soil Chemistry Research Group, Department of Plant and Soil Sciences, 152 Townsend Hall, University of Delaware, Newark, DE 19717-1303.

[b]Advanced Light Source, 10.3.2, Lawrence Berkeley National Laboratories, Berkeley, CA 94720.

For submission to the editorial board of Geochimica et Cosmochimica Acta

* Author to whom correspondence should be addressed.

Phone: +1 302.831.8435

FAX: +1 302.831.0605

Email: mgrafe@udel.edu

Abstract – A soil contaminated industrially by copper chromated arsenate (CCA) was investigated to elucidate the effects of co-contaminating metal cations (Cr, Cu, Zn) on the solid phase speciation of As. Micro-focused, synchrotron based X-ray fluorescence (μSXRF) mapping and micro-focused X-ray absorption spectroscopy (μXAFS) were used to glean detailed *in-situ* information about the spatial distribution of arsenic (As) in relation to other metals and to probe the coordination environment of As. The upper (LM-A) and lower (LM-B) 20 cm of the soil profile were investigated. The soil was limed and pH values ranged between 7.0 and 7.5. Phosphate and NH_4-oxalate/ ascorbic acid solutions were the most effective desorbing agents for As suggesting that most As was bound as inner-sphere complexes at the soil-water interface. Pearson correlations between As and Cr, Cu and Zn ranged between 52 and 91 per cent. With increasing depth, the As:Zn correlation was consistent (~81 – 91 per cent), but the As:Cr correlation decreased by ca. 21 per cent (89 – 68 per cent), while the As:Cu correlation increased by 25 per cent. (52 – 77 per cent). Micro-XAFS analysis suggested that As occurred dominantly as As(V) in LM-A and LM-B, but isolated spectra showed the presence of As(III) ocurring as AsO_3 and orpiment (As_2S_3). Abstract factor analysis of 29 sample spectra from LM-A and LM-B suggested that As occurred mainly as Cu and/ or Zn - arsenates surface clusters on Al and Fe oxides as well as fully precipitated metal-arsenate phases. Linear least-squares combination fit analysis (LLSF) of individual soil spectra suggested that more than 84 per cent of As occurred as metal-arsenate clusters or co-precipitated phases of either mixed Cu-Zn-, Cu- or Zn-arsenates throughout the upper 40 cm. In LM-A, mixed Cu-Zn arsenate phases were more abundant than Cu-arsenates and Zn-arsenates. In LM-B Cu-arsenates were more abundant than mixed Cu-Zn, and Zn-

arsenate sorption phases. With increasing depth, Zn-arsenate sorption complexes became more abundant. The remaining 16 per cent of As solid phases unaccounted for by mixed metal-arsenates were mostly adsorbed As(V) surface complexes on Fe and Al-oxides.

Key words: CCA, copper, zinc, arsenic, co-contamination, precipitates, μSXRF and μXAFS, abstract factor analysis, PCA.

1. INTRODUCTION

Arsenic (As) is a highly toxic element that has been released into the environment by anthropogenic processes and weathering of As bearing minerals (Welch et al., 2000; Oremland and Stolz, 2003). Arsenic contamination occurs commonly in areas in which metal contamination is the prevalent problem due to the refinement of common parent materials or the application of mixed metal-arsenic substances (acid mine drainage, smelter wastes, pesticides, chromated copper arsenate, aka CCA) (Tamaki and Frankenberger, 1992; Smith et al., 1998; Hingston et al., 2001).

In well aerated environments, As exists primarily as the oxo-acid, arsenate (as As^{5+} = $H_nAsO_4^{(n-3)}$ = As(V) = arsenate). The solid phase speciation of As(V) on various Fe and Al (hydr)oxides has been extensively characterized and assumed to be primarily a 2D adsorption process in which a ligand exchange mechanisms result in the formation of dominantly bidentate binuclear As (V) species on the metal oxides (Waychunas et al., 1993; Fendorf et al., 1997; Grossl et al., 1997; Ding et al., 2000; O'Reilly et al., 2001). Adsorbed As(V) is more stable near its first pK_{a1} (2.24,(O'Neill, 1990)),

D- and p- transition and heavy metal cation (Co^{2+}, Ni^{2+}, Cu^{2+}, Zn^{2+}, Cd^{2+}, Pb^{2+}) sorption complexes on metal-oxides are more stable in near neutral pH environs (Stumm, 1992; McBride, 1994; Sparks, 2002). Unlike As(V), metal species in soil suspensions may undergo 3D sorption processes possibly involving ions from the soil surface (surface precipitates) or they form as a result of local oversaturation (precipitation) especially as the pH is increased and the hydrolysis constants of the metals are approached, which is why liming is sometimes used as a remediation strategy. However, the increased pH induced by this treatment could result in the increased bioavailability of arsenate (V).

The incorporation of As(V) tetrahedra as ligands into the structure of metal-hydroxide precipitates may be an important reaction mechanism by which As(V) is or could be immobilized in the environment. In minerals such as olivenite ($Cu_2AsO_4(OH)$) or adamite ($Zn_2AsO_4(OH)$), As(V) acts as a distinct insular or link unit to stacks of metal-polyhedra. Neo-formation of similar amorphous phases via the formation of surface precipitates and clusters, however, has to date not been proven or shown to occur in contaminated and natural environments. There is some evidence that As(V) is re-incorporated into ferric precipitates (scorodite, schwertmanite) and jarosite in mine tailings of gold and arseno-pyrite mines and sulfur springs suggesting that As and Fe^{3+} readily form precipitate phases in co-contaminated environments (Waychunas et al., 1993; Waychunas et al., 1995; Foster et al., 1998a; Langner et al., 2001; Carlson et al., 2002; Ford, 2002; Paktunc et al., 2003). Alternatively, (Waychunas et al., 1993) suggested that As(V) inhibited the precipitation of ferrihydrite by binding to Fe-Fe nucleation sites (Manceau, 1995; Waychunas et al., 1995). Based on thermodynamic calculations, Sadiq (1997) suggested that in an acidified soil environment, Fe and Al-arsenates controlled As solubility, while at high pH, $Ca_3(AsO_4)_2$ controlled As solubility. Cadmium, Cu, Ni, Pb, and Zn-arsenates were less soluble than Ca arsenate and hence would not control As levels in soil solution. The formation of Cu-arsenates in CCA contaminated soils thus appears likely. Proper identification of the As solid phase is therefore paramount in order to predict which solid phases control As solubility, fate, and transport.

The objective of our study was to investigate the effects of co-contaminating metal cations on the solid phase speciation of As in a copper chromated arsenate

contaminated soil. To accomplish our goal, it was important that a) the soil samples were investigated *in-situ* without major alteration by chemical treatments, and b) arsenic and metal phases could be effectively delineated by micro-spectroscopic analysis.

The isolation and identification of possible metal-arsenate precipitates cannot be accomplished with traditional (macroscopic) speciation techniques (sequential extraction, stirred flow experiments, replenishment desorption), because they lack spatial resolution below the field scale. In addition, chemical changes may be induced by the desorbing agent altering the original speciation of As in the soil. Also, bulk-spectroscopic techniques such as infrared or X-ray absorption spectroscopy may not be capable of ascertaining the existence of metal-arsenate precipitates, because they probe a large area (typically, ~ 2*10mm) in which minor phases are undetectable (Bertsch, 1998; Manceau et al., 2002). Therefore it was critical to this investigation to have at least the following three elements: 1) a way to delineate and locate elemental occurrences over a specific area; 2) to do so with a high degree of spatial resolution (scale of μm to nm preferable); and 3) to be able to follow up on the spatial investigation with an *in-situ* spectroscopic probe that could collect spectroscopic data at high signal to noise ratio at a similarly μm to nm spatial resolution. These conditions may be fulfilled by use of micro-focused synchrotron based X-ray fluorescence (μSXRF) and X-ray absorption spectroscopy (μXAS). These micro-spectroscopic tools have been successfully employed in the characterization of Ni and Zn-smelter contaminated surface and subsurface soils and dredged sediments using μSXRF and μXAS techniques in combination with principal component analysis and linear least-square combination fit analysis (LLSF) (Manceau et

al., 2000a; Manceau et al., 2000b; Isaure et al., 2001; Roberts, 2002; Scheinost et al., 2002).

2. MATERIAL AND METHODS

2.1. Soil Characterization

The soil samples used in this study were collected from a former timber/ lumber treatment site (shut down in 1953) near the University of Florida (Gainesville, FL) from depths of 0-20 cm (LM-A) and 20-40 cm (LM-B), and sealed into 5 L plastic buckets. The fractions were analyzed for total metal ion content by HNO_3 digestions, soil pH, particle size analysis, organic matter content (loss on ignition, LOI), and cation exchange capacity (CEC) (pH 7 and pH 5.5) (Jackson, 1956). The major primary and secondary clay minerals were identified by bulk X-ray diffraction using standard procedures (Jackson, 1956). The results of the soil characterization are summarized in Figure 1.

2.2. Replenishment Desorption Study

A replenishment desorption study was carried out by suspending ca. 0.30 g of either LM-A or LM-B soil in 30ml desorbing solution and shaking the suspensions for 20, 30min, 1hr, 2x2hrs, and one 24hr period. After each shaking period, the suspensions were spun down at 12,000 rpm for 10 min and an aliquot was removed from each centrifuge bottle for ICP analysis of As, Zn, Cu, Cr, Fe, Al, and Mn. The choice of desorbing agents and their replenishment were based on considerations reported by

(Tessier et al., 1979; Rapin et al., 1986). The desorbing agents were 0.01M $CaCl_2$ solution, 0.25M Na_2HPO_4 solution or a 0.20M $(NH_4)_2$-oxalate/ 0.10M ascorbic acid solution. The $CaCl_2$ solution removes weakly bound or outer-sphere bound ions, the phosphate solution removes inner and outer-sphere adsorbed AsO_4 species, and the oxalate/ ascorbic acid solution as a strong reducing agent will convert amorphous Fe^{3+} (s) to Fe^{2+} (aq.) and subsequently chelate the dissolved ferrous iron as oxalate compounds. This treatment removes inner-sphere complexes, specifically those bound to amorphous iron and possibly aluminum oxides. Similar experiments have been carried out by other researchers with similar treatments and evaluations of their effects (Sun and Doner, 1996; Daus et al., 1998; La Force et al., 2000; Balasoiu et al., 2001; Scheinost et al., 2002). Each treatment was carried out in triplicate. The results were averaged and graphically summarized in Figure 2.

2.3. μSXRF and μXAFS Data Collection

Micro-focused (synchrotron-based) X-ray fluorescence (μSXRF) spectroscopy and micro-focused X-ray absorption fine structure (μXAFS) spectroscopy experiments were conducted at beamline 10.3.2 of the Advanced Light Source (Lawrence Berkeley National Laboratories, Berkley, CA), the operation of which is discussed by (Manceau et al., 2002) and (Marcus et al., 2004). This beamline provides a monochromatic beam spot whose size may be varied between 16x7 and 5x5μm^2 (HxV). For μSXRF, the sample is scanned under this probe while fluorescent X-rays are monitored by a 7-element Ge detector. For μXAFS, the energy is varied while the sample stays fixed with the beam at a point of interest. Energy calibration was done using an arsenate standard (Na_2HAsO_4,

10 wt. % in BN, As (V) K-edge taken as 11.874 KeV at the inflection point). The samples were investigated either as 30 μm thin sections (embedded in 3M Scotchcast electrical resin), or as powder films on kapton tape. Both size fractionated and un-fractionated powder samples were investigated. Size fractionated samples were obtained by settling in 80mM sodium hexametaphophate for 2hours following standard procedure. A core of the settled out soil was then divided into three sections by visual inspection and freeze-dried: a sand only section (Sand) , a sand-silt-clay mixture (SSCMIX), and a silt-clay fraction (SiCl).

Elemental maps were obtained by scanning successively smaller areas and regions of interest containing high fluorescence counts of arsenic and other elements of interest. The pixel size varied between 20x20 and 5x5 μm depending on the total area of a map. We recorded the following fluorescence signals: K Kα, Ca Kα, Ti Kα, Cr Kα, Mn Kα, FeKα/MnKβ, FeKβ, Ni Kα, Cu Kα, ZnKα/CuKβ, ZnKβ, As Kα, and As Kβ. The Kβ fluorescence counts of several elements were recorded in order to discriminate against the effects of overlapping signals from other elements (e.g. Cu Kβ and Zn Kα). During a mapping run, the energy of the beam was set to mid range (12.224 KeV) of the (subsequent) XAFS experiment. The fluorescence yield was normalized against the incident intensity I_0 and the dwell time. Scatter plots of the fluorescence counts between two elements were derived from the fluorescence information contained in each pixel for each map and a linear Pearson correlation coefficient was calculated in order to evaluate the co-occurrence between two elements (Table 1, Fig. 3, Fig. 4a, Fig.4b).

Between one and three suitable spots for As K-edge XAFS spectroscopy were selected per map. Arsenate K-edge (11.874 KeV) XAFS data were recorded from 200 eV

below to 750 eV above the edge energy. At least one million counts per point were collected for sample spots and three million counts/point for reference standards collected at this beamline. This resulted in at least two or three XAFS scans being collected for each spot.

2.4. XAS References

2.4.1. Preparation Procedures

A large number of reference phases were prepared to help in the data analysis. Four types of XAS references were prepared: aqueous, sorption, homogeneous precipitates and mineral standards (mineral standards obtained from *Excalibur*^{TM}). The sorption standards were prepared at either pH 4 or 7 by hydrating a specific amount of goethite or gibbsite in 0.01 M NaCl. The suspension concentration was normalized with respect to the specific surface area of each mineral such that the amount of surface area provided in each suspension was equal in all reaction vessels. All suspensions were hydrated for at least 24 hrs prior to reaction. The reaction pH was maintained using a Metrohm pH stat and 0.10 N HCl or NaOH as needed prior to the addition of the sorptives. The pH was held constant with the pH stat during and after the addition of the sorptives. Sorptives were added to the suspensions from prepared stock solutions. When sorptives were added incrementally, the equilibration period between each new addition was at least 30 min and until the pH had stabilized. Once all increments had been applied, the reactions were allowed to equilibrate an additional 24 hrs. Homogeneous precipitates were prepared in pH 7, 0.01M NaCl solutions using metal and arsenate stock solutions

such that the brief initial concentration in solution of each reagent was equal to 10mM. Table 2 provides an overview of the preparation procedure and subsequent nomenclature of the samples.

2.4.2. XAFS Data Collection.

Reference As K-edge EXAFS (Extended X-ray Absorption Fine Structure) spectra of model compounds and sorption samples synthesized in the laboratory were collected at beamline 10.3.2 (following the procedure described above) and beamline X11-A of the National Synchrotron Light Source (Brookhaven National Laboratories, Upton, NY). On beamline X-11A, the monochromator consisted of two parallel Si (111) crystals with vertical entrance slit opening of 0.5mm (O'Reilly et al., 2001). The (I_0) ionization chamber was filled with 10 and 90 percent Ar and N_2, respectively. Sorption samples were oriented at 45^o to the incident beam and the fluorescence detector for maximum fluorescence signal acquisition. The fluorescence signal was collected with a Kr-filled Lytle cell detector at room temperature. The unfocused beam was detuned by 30 percent in I_0 to reject higher harmonics. For signal optimization and removal of elastically scattered radiation, the fluorescence signal was filtered by a germanium foil (6 absorption lengths thick), one to two sheets of aluminum foil and Soller slits. The monochromator angle was calibrated to Na_2HAsO_4 as described above for the ALS, except that its spectrum was acquired simultaneously with that of the sample so as to control for drifts in the monochromator. At least three scans were collected for each sample. Homogeneous precipitates, mineral and aqueous standards (Na_2HAsO_4 (aq.)) were scanned in transmission mode. At 10.3.2, a mineral/ precipitate spot of appropriate

thickness was selected from a small fluorescence map to avoid overabsorption effects in the EXAFS.

2.5. Data Analysis

All data were initially analyzed using WinXAS 2.1 (Ressler, 1998) software package. Individual spectra were background corrected and normalized prior to averaging. The abscissa were converted from energy to photoelectron wave vector units (k = is the wave vector number with units of ~ $Å^{-1}$) by assigning the origin, E_0, to the first inflection point of the absorption edge. A cubic spline function consisting of no more than seven knots was applied in a linear least-squares fit over an average range in k-space (ca. 2 – 13 $Å^{-1}$). Fourier transformation (FT) of the raw $k^3\chi(k)$ function was performed over a consistent region in k-space (2.75 – 12.50 $Å^{-1}$) and an analog of a radial structure function (RSF) was obtained using a Bessel window function (β=4). The RSFs of all reference phases were Fourier filtered and back transformed for non-linear least-square shell fitting of individual shells. Structural parameters gleaned from this exercise were then used to perform a non-linear least-square multi-shell fit of the raw k^3-weighted χ function (Table 3).

The FEFF 7.02 code (Zabinsky et al., 1995) was used to calculate theoretical phases and amplitudes of single and multiple scattering paths for As-O, As-O-O-As multiple scattering, As-Fe, As-Zn, As-Cu, and As-Mn using input files based on the structural refinement of several different minerals. The choice of mineral was based on the composition of the reference phase. Generally, for sorption and homogeneous precipitated samples containing As and Fe only, we used mapimite ($Zn_2Fe_3[AsO_4]_3(OH)_4$

· $10H_2O$), due to the naturally occurring bidentate binuclear complex of As (V) with two edge-sharing Fe-octahedra. For samples containing As and Zn only, we used adamite ($Zn_2AsO_4(OH)$), for As and Cu, orthorhombic olivenite ($Cu_2AsO_4(OH)$), for As, Cu, and Zn, we used As substituted kipushite ($Cu_5Zn[PO_4, AsO_4]_2(OH)_6 \cdot H_2O$), for As, Cu, and Al, liroconite ($Cu_2Al[AsO_4](OH)_4 \cdot 4H_2O$), and for As, Zn, and Fe, we also used mapimite or ojuelaite ($ZnFe^{3+}{}_2[AsO_4]_2(OH)_2 \cdot 4H_2O$).

Up to four separate scattering paths were fit simultaneously. The number of permissible free-floating parameters for the Δk and ΔR values listed above is ca. 17 using the formula $N_{pts} = 2(\Delta k \Delta R/\pi)$ (Stern, 1993). During the fitting routine the coordination number (CN), the radial distance (R), and a common cross-correlated ΔE_0 value (phase shift) for all backscatters were allowed to vary. The mean square-root distance (σ^2) (measure of the disorder in the bond distance) of multiple-scattering paths (O-O-As) were constrained to be equal to that of the As-O distance. The disorders of second shell scattering paths were constrained to each other as well. A fixed amplitude reduction factor was set to unity and applied for each fit. Cross-correlation of σ^2 in the second shell is not uncommon in complex systems in which the metal neighbors vary (Manceau et al., 2000b). The inclusion of multiple-scattering (MS) events in EXAFS fitting for tetrahedral structures has been assessed previously (Sayers and Bunker, 1988; Pandya, 1994; Foster et al., 1998b; Ressler et al., 1999; Sherman and Randall, 2003). Multiple-scattering is most intense in the XANES (X-ray Near Edge Absorption Edge Fine Structure) energy region and the low *k*-space EXAFS region (2-5 $Å^{-1}$) where we observed distinct splitting of the first oscillation in *k*-space due to multiple-scattering. With respect to understanding As sorption in co-contaminated environments, knowledge about the position and

magnitudes of MS is important in order to avoid erroneous assignment of peaks in the FT functions to possible neighboring metals. Arsenate has tetrahedral coordination similar to CrO_4 and may be similarly rigid enough to support both collinear and noncollinear multiple scattering (MS) (Pandya, 1994). In radial structure functions, the noncollinear MS (we continue to use MS to represent noncollinear MS in this manuscript) appears often as a poorly resolved "buckle" feature which is often adjacent to the second shell features, often not well resolved and not always distinguishable in non-linear least-square shell fits (Pandya, 1994). In order to distinguish contributions of neighboring metal atoms from multiple scattering, the non-linear least-square multi-shell fitting was done first by fitting Fourier back-transformed second shells with metal atoms to observe their CNs and radial distances (no MS included, although some contributions were always apparent). The structural parameters thus obtained were adopted for an initial fit of the raw k^3-weighted $\chi(k)$ spectra without including MS to observe any changes in the second shell parameters through the inclusion of the dominant O contributions to the k^3-weighted $\chi(k)$-function. Next, we included a MS path and fixed the CN to 12 to observe the effects on the second shell parameters. Finally, the CN of the MS was allowed to vary to observe the effects on the multi-shell fit again. A MS event was only included in a fit if R_{MS} was between 3.00 and 3.20 Å. The CN_{MS} was either fixed to 12 if it exceeded a CN of 12 by more than 3, and otherwise it was allowed to vary according to its σ^2, which we correlated to the σ^2 of the average As-O distance. Hence, distortions in the tetrahedron, which don't allow for perfect multiple scattering ($CN_{MS} \sim 12$), were taken into account as we assumed that they would be induced by the sorption complex. The discussion on the appropriate inclusion of MS events in the fitting of environmental tetrahedral XAFS

patterns remains controversial; however, we believe that our approach begins to reconcile the effects of MS with respect to the second shell. Figure 5 shows the FT magnitude of the modulus and imaginary phase of three types of As(V) solid phases (A = aqueous, B = adsorbed, and C = mineral) with (A'-C') and without (A-C) the inclusion of a MS (O-O-As) path.

For oxidation state analysis of soil spectra, their XANES spectra were plotted to compare the position of the inflection point to reference standards (Figure 6). In addition, the first peak in the RSF, due to first ligand shell backscattering, was Fourier back transformed and a linear least-square fit was performed against Na_2HAsO_4, H_3AsO_3, and As_2S_3 reference spectra using beamline 10.3.2's linear combination fitting program (http://xraysweb.lbl.gov/uxas/Index.htm). The inclusion of more than one oxidation state required an improvement of the linear fit by 20 percent (Table 4).

2.5.1. Abstract factor analysis (AFA)

Abstract factor analysis (also known as principal component analysis) as a means to describe large data sets has been used previously by a number of researchers (Wasserman et al., 1999; Ressler et al., 2000; Manceau et al., 2002; Scheinost et al., 2002) and was conducted for experimental $k^3\chi(k)$ spectra (2.75 – 10.50 $Å^{-1}$) of LM-A (n = 13) and LM-B (n=16) using beamline 10.3.2 Principal Component Analysis software (available at http://xraysweb.lbl.gov/uxas/Index.htm, as are all the 10.3.2 analysis programs) (Table 5a). This procedure involved the reproduction of the data set (LM-A & LM-B) using abstract (mathematical, non-physical) factors, in which data points of experimental functions were reproduced as linear sums of product functions (i.e. the

abstract factors) (Malinowski, 1977). Principal component analysis (PCA) determined the number of abstract functions required to describe the complete set of experimental spectra (Figure 7A, Table 5a). Subsequently target transformation analysis was conducted to characterize the selected principal components (PCs) (Figures 7B-D, Table 5b). In target transformation, a known reference spectrum is tested by removing from it all signal not describable as a linear combination of the factors. The degree to which this operation alters the original test spectrum is measured by a SPOIL value (Malinowski, 1978; Manceau et al., 2002). A high SPOIL means that the reference being tested cannot be described as a sum of the factors and is therefore not a plausible component of the data. Meaningful SPOIL values range between 0 and 4.5 and were subdivided into quality criteria of: excellent ($0 \leq$ SPOIL < 1.5), good ($1.5 \leq$ SPOIL < 3), and fair ($3 \leq$ SPOIL < 4.5) (Malinowski, 1978). Identified reference spectra were then considered in the reference list of possible references for the linear least-square combination fit analysis (LLSF).

2.5.2. Linear least-square combination fitting (LLSF)

Linear least-squares combination fit analysis (LLSF) was conducted to reveal the identity of individual spectra using the beamline 10.3.2 linear combination fitting program. The badness-of-fit was evaluated by calculating a sum-square value of the fit involving the inclusion of the i^{th} component. In order for a second and third component/ reference spectrum to be considered, the fit had to improve by at least 20 per cent (Manceau et al., 2002). In order to avoid ambiguities introduced by the increasing noise at higher k, the fitted k-range was shortened from 12.50 $Å^{-1}$ to 10.5 $Å^{-1}$. Examples of the

LLSF analysis for LM-A and LM-B are presented in Fig. 8a and 8b, respectively. The complete LLSF analysis is presented in Table 6 and summarized as a ternary plot in Figure 9.

3. RESULTS

3.1 Soil Characterization

The investigated soil originated from an Arredondo–urban land complex with a taxonomic classification of a loamy, siliceous, hyperthermic Grossarenic Paleudult (Komar, 1999). Circa 85 per cent of the soil consisted of sand particles, 12% of the silt-sized fraction, and 3% of clay (Fig. 1). Bulk-XRD analysis revealed that quartz and kaolinite were the only crystalline soil components present (data not shown). These characteristics and the low organic matter content (2.9 vs. 1.2 weight per cent; LM-A and LM-B, respectively) are reflected in the low CEC of the soil. The low CEC (pH 7, 10 vs. 6 meq_c 100 g^{-1} soil, LM-A and LM-B, respectively) was directly related to the low OM content, which dropped similarly by half from LM-A to LM-B. Circa 1300 ppm Cu, 450 ppm Cr, and 900 ppm As were found in LM-A. Concentrations of Cu, Cr, and As were about 75% lower in LM-B than in LM-A. This investigation also revealed that the soil was contaminated with 700 ppm Zn in LM-A and 170 ppm Zn in LM-B. The Fe content in LM-A (14.6 ppt) dropped by 87 per cent (1.8 ppt) in LM-B. The Al content, however, was comparably stable dropping from 5.5 ppt to 3.8 ppt with depth. The Mn content was less than 100 ppm throughout the entire soil. The soil pH was between 7.0 and 7.5 as a result of $CaCO_3$ stabilization.

3.2. Replenishment Desorption Study

Desorption of As, Cu, Cr, Fe, Al, Mn, and Zn from LM-A and LM-B increased with increasing strength of the desorbing agent (Fig. 2). Zinc was the most labile ion and almost completely removed in the oxalate/ ascorbic acid treatment for both LM-A and LM-B after application of 6 pore volumes. Zinc desorbed more easily than As. The $CaCl_2$ solution removed less than 5 per cent As, however, the phosphate and oxalate/ ascorbic acid treatments removed ~ 50 and 90 per cent of As, respectively. Arsenic was not more or less stable in LM-A versus LM-B. Overall the individual ion fractions were quite resistant to desorption. After 24 hrs and 6 replenishments, only Mn did not desorb any further.

3.3. μSXRF

Micro-SXRF maps consist of an array of pixels which hold information about the fluorescence count of each specified element (As, Cr, Cu, Fe, Mn, Zn, etc.). The information that is stored in these pixels may be portrayed in two ways: 1) as a fluorescence map of one, two or three simultaneously featured elements, and 2) as a scatterplot of the counts from two elements. Scatterplots may be analyzed for correlation between the two elements by specifying a Pearson correlation (r). Figure 3 shows the Pearson correlations between As, Cr, Cu, Fe, Mn, and Zn as grey-scaled matrices for several powder-on-tape and thin section maps from LM-A and LM-B. Information from samples of non-uniform thickness such as powder-on-tape samples may cause false

correlations to appear in scatterplots, because bigger particles yield points on the scatterplot, which are radially displaced from those from smaller ones. This problem is illustrated in some of the powder-on-tape matrix plots, in which most fields are black, i.e. elements have false high correlation among each other (e.g., LM-B SSCMIX Map 2). In some cases though, the Pearson correlation coefficients from scatterplots of thin sections and powder samples were either equally uniform or equally random suggesting that the mapping area on the powder-on-tape samples was uniform enough in thickness (e.g., LM-A Map C, LM-A SSCMIX Map 1 or LM-B Maps A and B). With respect to information collected from thin section maps and the co-contaminating cations, Cr, Cu, and Zn, As:Cr and As:Zn correlations were between 80 and 100 percent and generally greater in LM-A than in LM-B. As:Cu correlations were lower in LM-A (~45 percent) than in LM-B (~ 75 percent) (Table 1).

Fluorescence maps complement the numeric interpretation by providing location specific information of the elements. Tri-, di-, and mono-colored fluorescence maps can be portrayed with the RGB (red, green, blue) color scheme, by assigning each “primary” color (red, green, blue) to a different element. When fluorescence signals from different elements overlap, the “primary” colors mix according to their fluorescence intensity and produce a secondary color: red + green = yellow, green + blue = cyan, blue + red = magenta, and red + green + blue = white. This is portrayed by the RGB color triangle in each map. The intensity scale is based on the grey scale, with white being most intense and black being the least intense. Prominent white spots in fluorescence AsZnCu maps reflected high correlation among the three elements (see Fig. 4a, Map A, spot 1) and was a common feature in AsZnCu tricolor fluorescence maps. Arsenic, Cr, Cu, and Zn often

accumulated band-like around Fe hotspots (Fig. 4a, Maps a-c). The cross-section featuring the arrow line in Map 'a' of Figure 4a shows how Fe fluorescence intensity ($I_{fl.}$) is greater on the left side of the particle, while the intensities of As, Cr, Cu, and Zn are greater on the right side of the particle (Fig. 4a, Frame 'd'). Quantification of the amounts of As, Cr, Cu, Fe or Zn cannot be made from these cross-sections, because the fluorescence signal of lower Z (atomic number) elements is absorbed to a greater extent in the sample itself than for higher Z elements. The fractions of the incident beam and output fluorescence depend on the atomic number of the element in question and on the amount and identity of all other elements present. Micro-EXAFS data were subsequently collected from spots marked 1, 2, and 3 in Map A of Figure 4a.

Often it is useful to combine information from scatterplots and fluorescence maps in order to differentiate between elemental hotspots on a map. This could be well illustrated with the information gathered from LM-B TS Map 2 by masking (isolating) different linear segments in a scatterplot and subsequently remapping the same area featuring only pixels included in the mask (Fig. 4b). A dual relationship between As and Zn was observed in this particular thin section map. Figure 4b, Map A shows a triangular frame with individual magenta hotspots in its center suggesting strong AsCu mixing in these spots, while the rim is both lighter and more yellow suggesting a greater influence from Zn and As. Pixels in mask 1 were associated with the AsCu hotspots within the rim, while the rim pixels where associated with Mask 2. The differing slopes of the linear segments in the scatterplots suggested that a different solid phase may exist on the rim from the hotspots within the rim. Micro-EXAFS data were subsequently collected on spots marked 1, 2, and 3.

3.4. X-ray Absorption Spectroscopy

3.4.1. Reference Spectra

Traditional numerical analysis or non-linear least-squares multi-shell fitting analysis was conducted on selected reference standards (see Table 2 for reference phase nomenclature, see Table 3 for summary of structural parameters). Fitting was performed on raw k^3-weight χ-functions with special attention to three features: Identity and magnitudes of the first (ligand) and the second shell, and multiple scattering (MS). To observe MS, the k^3-weight χ-functions were cut between 2.75 and 13.00 $Å^{-1}$. At low wavenumbers (2-5 $Å^{-1}$) in k^3-weighted $\chi(k)$ spectra, we observed distinct splitting of the first oscillation due to multiple-scattering. The coordination number (CN) and radial distance (R) of the first ligand shell were ca. 4.5 and 1.69 Å suggesting tetrahedral coordination of oxygen atoms around As. The CN_{MS} was variable, ranging from 6.4 (Mansfieldite) to >> 12. Figure 5 shows the FT magnitude of the modulus and imaginary phase between two and four Ǻ (uncorrected for phase shifts) of three types of As(V) solid phases (A = aqueous, B = adsorbed, and C = mineral) with (A'-C') and without (A-C) the inclusion of a MS (O-O-As) path. The discrepancy between fitted and experimental data in the absence of a MS suggested that contributions from some neighboring backscattering atoms were missing in the fit. These contributions were best modeled with multiple O-O-As scattering, which was a consistent feature in the FT of all examples at ~ 2.4 Ǻ. The backscattering contributions at this distance may be overlapped by additional

neighboring metal cations. This is apparent from the fits for Goe-7.8, and was observed in several other spectra, e.g. Gib 7.3, Goe 7.0-7.8. These overlapping backscattering contributions stem mostly from corner-sharing sorption complexes (^{2}C) with Al and/ or Cu at ~ 3.15 Å.

Differentiation of the second shell parameters of all possibly neighboring metal atoms (Fe, Al, Cu, Zn) was generally possible. Bidentate binuclear complexes with Fe and/or Zn could generally be distinguished from each other by noticing a distinct increase in R beyond 3.30 Å. Copper could be identified by a shift in the second shell to lower R, between 3.14 and 3.24 Å. The magnitudes of the CN in the second shell of sorption samples varied between 1.3 and 7.8. Sample Goe-7.4, for example, with CN of 7.8 was previously identified as an adamite-like surface precipitate (Gräfe et al. 2004). In sample Gib.-7.4, where the sum of all second shell CNs exceeded 3, is probably representative of small surface clusters in which As bonds to Cu and/ or Zn and to the sorbent (gibbsite). In sample Gib.-7.3, MS and Al-As contributions strongly overlapped, and a fit involving both MS and Al in the second shell was not possible. The magnitude of the second shell CN_{As-Al} was 1.6 (see values in parentheses) suggesting that a similar surface surface cluster had formed as in sample Gib.-7.4. A definitive characterization of these surface complexes requires complimentary XAFS analysis at the Cu and/ or Zn K-edges, which was beyond the scope of this study (Gräfe et al., 2004).

Homogeneous precipitates and mineral standards show that the magnitude of the CN should exceed or be nearly four. A noticeable exception is the HZAP, where the second shell σ^2 was significantly reduced by the inclusion of MS in the fit. A possible independent third second shell, however, could not be fit. The residuals for all fits varied

according to the amount of noise in the individual spectrum as all fits were performed on raw k^3-weigthed χ-functions.

3.4.2. Oxidation State Analysis.

The oxidation state of As in the soil was evaluated initially by visual inspection of the μXANES spectra (Fig. 6) and linear least-squares fitting of Fourier back transformed first shell peaks in RSFs against standards of arsenate (As(V)), arsenite (As(III)) and orpiment (As_2S_3) (Table 4). The position of the edge-jump of most spectra suggested that As(V) was the dominant oxidation state of As in the soil. However, there were differences noticeable from several spectra such as those in Figure 6. Changes in the positions of the whiteline (point of maximum absorbance in the energy spectrum) in the spectra suggested mixtures of oxidation states and possible contributions from different ligands other than oxygen. LLSF analysis of the Fourier back-transformed first ligand shells was conducted to confirm oxidation states based on phase shifts in k^3-weighted $\chi(k)$ functions stemming from variable As-O or As-S distances depending on the As oxidation state and ligand (Table 4). LLSF analysis determined that As(V) was dominant in LM-A and LM-B (>93 per cent). Spectra collected from thin sections of LM-A commonly contained As(III), which may be an artifact of the resin and the beam. Hence, these values were not considered in the reported average. Arsenite was present less than one percent in LM-A, but in LM-B, ca. five percent As(III) were present. Less than one percent As_2S_3 were present in either depth fraction. The range of As(III) and As_2S_3 present in LM-B was between 10 and 23 percent with an average of 17 percent.

3.3.3. Abstract Factor Analysis

The minimum number of principal components (PCs) required to reproduce a larger data set was evaluated by the IND local minimum theory and was obtained for 29 sample spectra from 5 PCs (Malinowski, 1977). By visual inspection of the PCs (weighted by eigenvalue), PC#5 did not appear sufficiently EXAFS-like to justify its inclusion (Figure 7A). Because the IND determination method is not fully accepted (Manceau et al., 2002), and visual inspection is too subjective, we compared the IND method with the marginal decline of the eigenvalues. The change of the eigenvalues was consistently smaller with increasing PC # up to the 5th PC corroborating the suggestion of the IND method (Table 5A). In addition, we compared the marginal improvement of the fit total (normalized sum-square total (NSS-tot.)) by successively including the next PC. The inclusion of PC#5 improved the fit by a greater margin than the previous inclusion of PC#4. This appeared unjustified, because the eigenvalue of PC#5 is ca. 8.7 percent smaller than that of PC 4 (Table 5A). Since eigenvalues rank PCs according to their importance to reproduce a data set, we concluded that the minimum number of PCs required to properly reproduce the data set was more likely four than five.

Target transformation of the selected first four PCs with references of known identity showed that our reference database did not contain spectra that would fall into the SPOIL category excellent (SPOIL $\leq$ 1.5). The majority of reference standards had a SPOIL value between 1.7 and 3.0 (see Figure 7 B-D and Table 5B). The identities of these references show that mixed CuAs, CuZnAs, and ZnAs sorption, precipitate, and

mineral phases obtained the lowest SPOIL values suggesting that As was largely complexed by the co-contaminating metal cations.

3.3.4. Linear least-square combination fit analysis (LLSF)

Linear least-square combination fitting of unknown spectra from LM-A and LM-B was conducted over a *k* range of 2.75 to 10.50 $Å^{-1}$ (see examples in Fig. 8a and 8b for LM-A and LM-B respectively). All LLSFs are presented in Table 6 and a ternary plot summarizes the LLSF results in Figure 9. The list of known reference compounds for the LLSF was initially limited to the spectra identified by the target transformation with SPOIL values below 3. The addition of another reference spectrum into the linear fit was only warranted if the sum-square value (badness-of-fit) decreased by at least 20 per cent. In order to avoid disregarding minor phases not identified in the PCA/ TT, the reference list was expanded to include references with a SPOIL rating of 'fair' (4.5), and subsequently opened to all As reference spectra. This procedure showed that there were indeed minor phases that can be overlooked in the PCA/ TT (e.g. allactite and olivenite). All sample spectra were identified using linear 2 component fits except in one case. The average sum-square values were ~ 2.8 and 4.7 per cent in LM-A and LM-B, respectively, which is in good agreement with the NSS-tot. value for two to three PCs (see Table 5A). The reference spectra used in the LLSF analysis may be summarized into three types of metal-arsenate combinations: CuAs, CuZnAs, and ZnAs (Figure 9). They represented 83 and 93 per cent of the As solid phase speciation in LM-A and LM-B, respectively, with the remaining 17 and 7 per cent being composed of various mineralized complexes including mansfieldite, scorodite, allactite, and 2D As(V) adsorption complexes on Fe

and Al-oxides (mostly phases not identified in the PCA/ TT). In LM-A, the mixed CuZnAs solid phase was more abundant than the CuAs solid phase than the ZnAs solid phase (42 vs. 34 vs. 8 per cent, respectively). The order and abundance of these three phases changed with increasing depth. In LM-B, the CuAs solid phase (42 per cent) was more abundant than the CuZnAs solid phase (33 per cent). The least abundant phase was the ZnAs solid phase, but its occurrence increased from 8 to 18 percent with depth. Interestingly, many of the observed Cu, Zn and mixed CuZn-arsenate precipitated phases occurred in connection with Cr_2O_3, which we used as a sorbent material in some of the 10mM Cu, Zn, As(V) precipitates. The three major solid phases may be represented in a ternary plot of end-members/ species CuAs vs. the combined Zn/Me-As species vs. CuZnAs species. The two main mixtures occur between Zn/Me-As species and either CuAs or CuZnAs species showing that CuAs and CuZnAs rarely form mixtures together. Despite these numerical differences, P-values from a paired t-test suggested that one is incorrect in stating that the two means between of each category (CuAs, Zn/Me-As, and CuZnAs) for LM-A and LM-B are different (Fig.9).

4. DISCUSSION

4.1. The data in perspective

This work differed from recent studies using similar investigative and analysis techniques for Zn and Ni speciation in smelter contaminated soils and dredged sediments (Manceau et al., 2000a; Isaure et al., 2001; Roberts, 2002; Scheinost et al., 2002), because the current study is concerned with identifying solid phases formed from initially

aqueous contaminants, while other studies have been investigating the dissolution and redistribution of metals in varying solid phases. This study is also novel in its specific concern over the role of co-contaminating metal cations on As solid phase speciation. Recent studies of As in mine wastes and processed slags have employed the traditional non-linear least-square multi-shell fitting technique from both bulk and μEXAFS data (Foster et al., 1998b; Carlson et al., 2002; Jing et al., 2002), but did not touch upon the role of present co-contaminating metal cations in As solid phase speciation. Paktunc et al. (2003) showed that As sorption complexes formed on Fe-oxyhydroxides with Ca in both submerged and exposed mine tailings that were subjected to various column leaching tests. Both bulk and μEXAFS data were collected and analyzed using the traditional numerical, non-linear least-square fitting routine. Manceau et al. (2002) pointed out that the traditional numerical EXAFS analysis methods are not necessarily appropriate for heterogeneous samples, because of the great variability of solid phases forming within distances of less than several nano and micro-meters, their overlap under focused and unfocused beams, and the subsequent overlapping of EXAFS contributions stemming from various sorption states. In addition, minor phases in a sample may go undetected, but may constitute an important fraction with respect to bio-availability. Our results fully corroborate these claims and demonstrate the central role that co-contaminating metal cations play in the solid phase speciation of As (see e.g., Fig. 4a, 4b & 8a, 8b).

Linear elemental correlations and μSXRF maps suggested that manganese and iron played an equally important role in the solid phase partitioning of As in this soil. Birnessite (δ-MnO_2) is a well known oxidant of As(III) in soils and generally not known to sorb significant quantities of As(III) or As(V) due to the low point of zero charge

(Stumm, 1992; Scott and Morgan, 1995; Nesbitt et al., 1998; Tournassat et al., 2002). The accumulation of As in Mn rich areas may have therefore occurred by way of attraction to other cations such as Zn and Cu, which were equally correlated to Mn and Fe. The lack of a single linear relationship between two elements does not mean that no relationship exists at all. This is corroborated by the As:Zn correlation plot in Figure 4b showing two separate linear relationships. LLSF analysis results showed that Fe and Al acted in numerous occasions as possible nucleation sites for As, Zn, Cu, and Cr co-sorption.

Arsenic as expected occurred mostly as As(V) given the sandy soil profile, the absence of water-logged conditions, and the original application of As_2O_5 (Bull and Harland, 2001). Interesting is the appearance of ca. 5 percent As(III) in LM-B. Circa 32 percent of the EXAFS spots investigated in LM-A and LM-B contained some amount of As(III) or As_2S_3 ranging between 4 to 23 per cent. This shows that there are isolated regions in well-aerated soils in which As(III) speciation is favorable and which may also occur as sulfide species. This may be influenced by localized OM fractions. (Redman et al., 2002) suggested that As(V) was reduced in the presence of dissolved organic matter in hematite suspensions. Balasoiu et al. (2001) found similar As(V) to As(III) ratios (95:5) in artificially CCA contaminated soils ranging from highly mineral to highly organic soils, with the fraction of As(III) increasing towards the organic soils.

Bull et al. (2000) examined CCA treated wood with bulk EXAFS spectroscopy showing that As(V) binds to chromium and copper. Several reviews and studies of CCA leaching behavior from treated wood and CCA fixation in soils have been published, but no attempts have been made to determine the coordination environment of the

contaminants in soils (Kazi and Cooper, 2000; Kazi et al., 2000; Balasoiu et al., 2001; Stevanovic-Janezic and Cooper, 2001; Stevanovic-Janezic et al., 2001; Kazi et al., 2002). Principal component, target transformation and LLSF analyses suggested that As was bound in the soil as a mixture of metal-arsenate sorption complexes and precipitates. These results are the first spectroscopic-statistical evidence of metal-arsenate sorption phases speciation in soils influenced by the co-contaminating metal cation fraction (Cu, Zn, Cr). A likely and important factor contributing to the formation of the precipitated phases was the neutral to alkaline pH environment. The effect of pH on metal-arsenate retention has recently been studied by (Gräfe et al., 2004) showing that the formation of zinc-arsenate precipitates at the goethite-water interface is favored in neutral than acidic pH. While the results from LLSF, linear elemental correlations, and μSXRF maps agreed well, one should notice that the best correlated pair, ZnAs, was not the most abundant As solid phase present, which suggests that one should not make immediate inferences on the solid phase based on μSXRF maps or spatial correlations. In comparison to the results from micro-spectroscopy, it becomes evident how limited the information stemming from macroscopic desorption studies was. The macroscopic data does however suggest that the application of phosphate and strongly chelating anions (e.g., EDTA) is likely detrimental to the stability of the metal-arsenate complexes in this soil. Hence, use of the contaminated site for regimented crop growth with vigorous fertility programs should be avoided.

4.2. Environmental Aspects

Traditionally there have been three CCA formulations (A, B, and C) in which the elements Cu, Cr(VI), and As(V) were applied as solutions to the wood. The per cent content of the mixtures is distributed on average into ca. 20 per cent CuO, 35 to 65 per cent CrO_3, and 16 to 45 percent As_2O_5, thus CCA formulations contain more Cr than As than Cu (Hingston et al., 2001). This distribution is exactly opposite to the total concentrations of Cu, Cr, and As found in LM-A or LM-B (Figure 1). Balasoiu et al. (2001) showed that for mechanical mixtures of soils ranging from highly mineral soils to highly organic soils, the ratio of total Cu:Cr:As retained in the soil after sequential extraction was similar to the initial application ratio of Cu, Cr, and As. It is therefore possible that As and Cr were leached in greater proportion from the soil than copper. As redox sensitive elements, the reactivity of As(V) and Cr(VI) is greater than that of the relatively inert As(III) and Cr(III). Upon application to the wood, Cr(VI) undergoes reduction likely forming Cr(III) (Hingston et al., 2001). Independent μXANES investigation of Cr's oxidation state at room temperature failed to provide conclusive evidence of Cr's oxidation state probably due to radiation damage and the presence of OM in the sample. Trivalent chromium tends to precipitate out as an inert hydroxide phase and should be retained in the soil; hence, loss of chromium from our soil should be related to loss of Cr(VI). Chromate and arsenate adsorption complexes on variably charged surfaces have lower stability with increasing pH suggesting that the remediation strategy of increasing pH to stabilize Cu (and Zn) lead to increased As and Cr desorption and leaching. The remaining As fraction, however, reacted with the Cu, Zn and Cr to form co-sorbed phases and precipitates.

5. CONCLUSIONS

Arsenic solid phase speciation in a soil heavily contaminated with other metals (Cu, Zn, Cr) was distinctly related to the same metal contaminants. Our study showed that mixed metal-arsenate phases accounted for up to 93 per cent of the As solid phase in the upper 40 cm of the soil. The effect of liming may have increased the leaching rate of As and Cr through the sandy soil profile but independent investigations on model systems are warranted to confirm this hypothesis. The role of Fe, Al, and Mn-oxides needs to be re-evaluated in situations in which soluble metals (e.g., Co, Ni, Cu, Zn, Cd, Pb) are present with As in soil solution. In many contaminated environments, this is the case (Williams, 2001). The formation of stable precipitated phases is from a remediation and clean-up standpoint favorable as it offers alternative options to costly excavation/ landfilling practices (e.g. phytoremediation). Basic research is needed to identify the underlying processes in the formation of metal-arsenate precipitates on ubiquitous metal sesquioxides such as goethite, gibbsite, and birnessite, and to test the stability of these precipitates in dissolution experiments.

Acknowledgements — We are grateful to the insightful comments and discussions with Dr. M. Nachtegaal and David McNear formerly and currently of the Environmental Soil Chemistry Group and (#) anonymous reviewers. We would like to thank Dr. A. Lanzirotti and W. Rao for their support while collecting the initial μSXRF and μXANES data at X26-A and Dr. K. Pandya for her support during XAFS data collection on reference standards at X11-A (both NSLS). We would like to thank Dr. L. Ma for her assistance

in obtaining the soil fractions from the CCA contaminated soil. Markus Gräfe appreciates a University of Delaware Competitive Academic Fellowship funding his research.

REFERENCES

Balasoiu C. F., Zagury G. J., Deschenes L. (2001) Partitioning and speciation of chromium, copper, and arsenic in CCA-contaminated soils: influence of soil composition. *Sci. Tot. Environ.* ***280***(1-3), 239-255.

Bertsch P. M., and D. B. Hunter (1998) Elucidating fundamental mechanisms in soil and environmental chemistry. The role of advanced analytical, spectroscopic and microscopic methods. In *Future prospects for soil chemistry*, Vol. 55 (ed. D. L. S. P.M. Huang, and S.A. Boyd). Soil Sci. Soc. Amer. Spec. Publ., Madison, WI. pp. 103-122.

Bull D. C., Harland P. W. (2001) The chemistry of chromated copper arsenate - III. Recovery of arsenic content from treatment plant sludges. *Wood Sci. Technol.* ***35***(1-2), 137-141.

Bull D. C., Harland P. W., Vallance C., Foran G. J. (2000) XAFS study of chromated copper arsenate timber preservative in wood. *Journal of Wood Science* ***46***(3), 248-252.

Carlson L., Bigham J. M., Schwertmann U., Kyek A., Wagner F. (2002) Scavenging of as from acid mine drainage by schwertmannite and ferrihydrite: A comparison with synthetic analogues. *Environ. Sci. Technol.* ***36***(8), 1712-1719.

Daus B., Weiss H., Wennrich R. (1998) Arsenic speciation in iron hydroxide precipitates. *Talanta* ***46***(5), 867-873.

Ding M., de Jong B., Roosendaal S. J., Vredenberg A. (2000) XPS studies on the electronic structure of bonding between solid and solutes: Adsorption of arsenate,

chromate, phosphate, Pb^{2+}, and Zn^{2+} ions on amorphous black ferric oxyhydroxide. *Geochim. Cosmochim. Acta* ***64***(7), 1209-1219.

Fendorf S., Eick M. J., Grossl P., Sparks D. L. (1997) Arsenate and chromate retention mechanisms on goethite .1. Surface structure. *Environ. Sci. Technol.* ***31***(2), 315-320.

Ford R. G. (2002) Rates of hydrous ferric oxide crystallization and the influence on coprecipitated arsenate. *Environ. Sci. Technol.* ***36***(11), 2459-2463.

Foster A. L., Brown Jr. G. E., Tingle T. N., Parks G. A. (1998a) Quantitative arsenic speciation in mine tailings using X-ray absorption spectroscopy. *Amer. Mineral.* ***83***, 553-568.

Foster A. L., Brown Jr. G. E., Tingle T. N., Parks G. A. (1998b) Quantitative arsenic speciation of in mine tailings using x-ray absorption spectroscopy. *Am. Mineral.* ***83***, 553-568.

Gräfe M., Nachtegaal M., Sparks D. L. (2004) Formation of metal-arsenate precipitates at the goethite-water interface. *Environ. Sci. Technol.* ***submitted***.

Grossl P. R., Eick M., Sparks D. L., Goldberg S., Ainsworth C. C. (1997) Arsenate and chromate retention mechanisms on goethite .2. Kinetic evaluation using a pressure-jump relaxation technique. *Environ. Sci. Technol.* ***31***(2), 321-326.

Hingston J. A., Collins C. D., Murphy R. J., Lester J. N. (2001) Leaching of chromated copper arsenate wood preservatives: a review. *Environmental Pollution* ***111***(1), 53-66.

Isaure M. P., Laboudigue A., Manceau A., Sarret G., Tiffreau C., Trocellier P. (2001) Characterisation of zinc in slags originated from a contaminated sediment by

coupling mu-PIXE, mu-RBS, mu-EXAFS and powder EXAFS spectroscopy. *Nuclear Instruments & Methods in Physics Research Section B- Beam Interactions With Materials and Atoms* ***181***, 598-602.

Jackson M. L. (1956) *Soil chemical analysis - Advanced course*. University of Wisconsin, Madison, WI.

Jing C. Y., Meng X. G., Korfiatis G. P. (2002) Arsenic mobility in iron hydroxide sludge stabilized with cement. *Abstracts of Papers of the American Chemical Society* ***224***, 122-ENVR.

Kazi F. K. M., Cooper P. A. (2000) Kinetic model of CCA fixation on wood. Part I. The initial reaction zone. *Wood and Fiber Science* ***32***(3), 354-361.

Kazi F. K. M., Cooper P. A., Chen J. B. (2000) Kinetic model of CCA fixation in wood. Part II. The main reaction zone. *Wood and Fiber Science* ***32***(4), 442-449.

Kazi F. K. M., Cooper P. A., Ung T. Y. (2002) Kinetic model of CCA fixation on wood. Part III. Model validation. *Wood and Fiber Science* ***34***(2), 318-324.

Komar K. M. (1999) Phytoremediation of arsenic contaminated soils: plant identification and uptake enhancement. MS, University of Florida at Gainesville.

La Force M. J., Hansel C. M., Fendorf S. (2000) Arsenic speciation, seasonal transformations, and co- distribution with iron in a mine waste-influenced palustrine emergent wetland. *Environ. Sci. Technol.* ***34***(18), 3937-3943.

Langner H. W., Jackson C. R., McDermott R., Inskeep W. P. (2001) Rapid oxidation of arsenite in a hot spring ecosystem, Yellowstone National Park. *Environ. Sci. Technol.* ***35***(16), 3302 - 3309.

Malinowski E. R. (1977) Determination of the number of factors and the experimental error in a data matrix. *Anal. Chem.* ***49***(4), 612-617.

Malinowski E. R. (1978) Theory of error for target factor analysis with applications to mass spetrometry and nuclear magnetic resonance spectrometry. *Anal. Chim. Acta* ***103***, 359-364.

Manceau A. (1995) The mechanisms of anion adsorption on iron oxides: Evidence for the bonding of arsenate tetrahedra on free $Fe(O, OH)_6$ edges. *Geochim. Cosmochim. Acta* ***59***, 3647-3653.

Manceau A., Lanson B., Schlegel M. L., Harge J. C., Musso M., Eybert-Berard L., Hazemann J. L., Chateigner D., Lamble G. M. (2000a) Quantitative Zn speciation in smelter-contaminated soils by EXAFS spectroscopy. *Am. J. Sci.* ***300***(4), 289-343.

Manceau A., Marcus M. A., Tamura N. (2002) Quantitative speciation of heavy metals in soils and sediments by synchrotron x-ray techniques. In *Applications of synchrotron radiation in low-temperature geochemistry and environmental science*, Vol. 49 (ed. P. Fenter and N. C. Sturchio). Mineralogical Society of America, Washington D.C. pp. 341-428.

Manceau A., Schlegel M. L., Musso M., Sole V. A., Gauthier C., Petit P. E., Trolard F. (2000b) Crystal chemistry of trace elements in natural and synthetic goethite. *Geochim. Cosmochim. Acta* ***64***(21), 3643-3661.

Marcus M., A.A. M., Celestre R., Manceau A., MIller T., Padmore H. A., Sublett R. E. (2004) Beamline 10.3.2 at ALS: a hard X-ray microprobe for environmental and material sciences. *J Synch. Rad.* ***11***, 239-247.

McBride M. B. (1994) *Environmental Chemistry of Soils*. Oxford University Press, New York.

Nesbitt H. W., Canning G. W., Bancroft G. M. (1998) XPS study of reductive dissolution of 7 Å-birnessite by H3AsO3, with constraints on reaction mechanism. *Geochim. Cosmochim. Acta* ***62***(12), 2097-2110.

O'Neill P. (1990) Arsenic. In *Heavy Metals in Soils* (ed. B. J. Alloway). Blackie, London.

O'Reilly S. E., Strawn D. G., Sparks D. L. (2001) Residence time effects on arsenate adsorption/desorption mechanisms on goethite. *Soil Sci. Soc. Am. J.* ***65***(1), 67-77.

Oremland R. S., Stolz J. F. (2003) The ecology of arsenic. *Science* ***300***, 939-944.

Paktunc D., Foster A. L., LaFlamme G. (2003) Speciation and characterization of arsenic in Ketza River mine tailings using X-ray absorption spectroscopy. *Environ. Sci. Technol.* ***37***(10), 2067-2074.

Pandya K. I. (1994) Multiple-scattering effects in x-ray absorption fine structure: Chromium in a tetrahedral configuration. *Phys. Rev. B* ***50***(21), 15509-15515.

Rapin F., Tessier A., Campbell P. G. C., Carignan R. (1986) Potential artifacts in the determination of metal partitioning in sediments by a sequential extraction procedure. *Environ. Sci. Technol.* ***20***(8), 836-840.

Redman A. D., Macalady D. L., Ahmann D. (2002) Natural organic matter affects arsenic speciation and sorption onto hematite. *Environ. Sci. Technol.* ***36***(13), 2889-2896.

Ressler T. (1998) Winxas: A program for x-ray absorption spectroscopy data analysis under MS-windows. *J. Synchr. Rad.* ***5***, 118-122.

Ressler T., Brock S. L., Wong J., Suib S. L. (1999) Multiple-scattering EXAFS analysis of tetraalkylammonium manganese oxide colloids. *J. Phys. Chem. B* ***103***, 6407-6420.

Ressler T., Wong J., Roos J., Smith I. (2000) Quantitative speciation of of Mn-bearing particulates emitted from autos burning (methylcyclopentadienyl)manganese tricarbonyl-added gasolines using XANES spectroscopy. *Environ. Sci. Technol.* ***34***, 950-958.

Roberts D. R., A.C. Scheinost, D.L. Sparks (2002) Zinc speciation in a smelter-contaminated soil profile using bulk and microspectroscopic techniques. *Environ. Sci. Technol.* ***36***, 1742-1750.

Sadiq M. (1997) Arsenic chemistry in soils: an overview of thermodynamic predictions and field observations. *Water Air Soil Poll.* ***93***, 117-136.

Sayers D. E., Bunker B. A. (1988) Data Anlysis. In *X-ray Absorption: Principles, Applications, and Techniques of EXAFS, SEXAFS, and XANES* (ed. D. C. Koningsberger and R. Prins). John Wiley & Sons, NYC. pp. 211-253.

Scheinost A. C., Kretzschmar R., Pfister S. (2002) Combining selective sequential extractions, x-ray absorption spectroscopy, and principal component analysis for quantitative zinc speciation in soil. *Environ. Sci. Technol.* ***36***(23), 5021-5028.

Scott M. J., Morgan J. J. (1995) Reactions at oxide surfaces. 1. Oxidation of As (III) by synthetic birnessite. *Environ. Sci. Technol.* ***29***, 1898-1905.

Sherman D. M., Randall S. R. (2003) Surface complexation of arsenic(V) to iron(III) (hydr)oxides: Structural mechanism from ab initio molecular geometries and EXAFS spectroscopy. *Geochim. Cosmochim. Acta* ***67***(22), 4223-4230.

Smith E., Naidu R., Alston A. M. (1998) Arsenic in the soil environment: A review. In *Adv. Agr.*, Vol. 64, pp. 149-195.

Sparks D. L. (2002) *Environmental Soil Chemistry*. Academic Press, San Diego, CA.

Stern E. A. (1993) Number of relevant independent points in x-ray absorption fine structure spectra. *Phys. Rev. B* ***48***, 9825-9827.

Stevanovic-Janezic T., Cooper P. A. (2001) Characteristics of sludges produced by destabilization of CCA preservative solutions. *Holzforschung* ***55***(5), 471-477.

Stevanovic-Janezic T., Cooper P. A., Ung Y. T. (2001) Chromated copper arsenate preservative treatment of North American hardwoods - Part 2.: CCA leaching performance. *Holzforschung* ***55***(1), 7-12.

Stumm W. (1992) *Chemistry of the Solid-Water Interface*. Wiley, New York.

Sun X. H., Doner H. E. (1996) An investigation of arsenate and arsenite bonding structures on goethite by FTIR. *Soil Sci.* ***161***(12), 865-872.

Tamaki S., Frankenberger W. T., Jr. (1992) Environmental Chemistry of Arsenic. In *Rev. Environ. Contam. Toxicol.*, Vol. 124. Springer-Verlag, New York. pp. 79-110.

Tessier A., Campbell P. G. C., Bisson M. (1979) Sequential extraction procedure for the speciation of particulate trace metals. *Anal. Chem.* ***57***(7), 844-851.

Tournassat C., Charlet L., Bosbach D., Manceau A. (2002) Arsenic(III) oxidation by birnessite and precipitation of manganese(II) arsenate. *Environ. Sci. Technol.* ***36***(3), 493-500.

Wasserman S. R., Allen P. G., Shuh D. K., Bucher J. J., Edelstein N. M. (1999) EXAFS and prinicipal component analysis: A new shell game. *J. Synchr. Rad.* ***6***(284-286).

Waychunas G. A., Rea B. A., Davis J. A., Fuler C. C. (1995) Geometry of sorbed arsenate on ferrhihydrite crystalline FeOOH: Reevaluation of EXAFS results and topological factors in predicting geometry, and evidence for monodentate complexes. *Geochim. Cosmochim. Acta* ***59***, 3655-3661.

Waychunas G. A., Rea B. A., Fuller C. C., Davis J. A. (1993) Surface chemistry of ferrihydrite: Part 1. EXAFS studies of the geometry of coprecipitated and adsorbed arsenate. *Geochim. Cosmochim. Acta* ***57***, 2251-2269.

Welch A. H., Westjohn D. B., Helsel D. R., Wanty R. B. (2000) Arsenic in ground water of the United States: Occurrence and geochemistry. *Ground Water* ***38***(4), 589-604.

Williams M. (2001) Arsenic in mine waters: an international study. *Environmental Geology* ***40***(3), 267-278.

Zabinsky F., Rehr J. J., Ankudinov A., Albers R. C., Eller M. J. (1995) Multiple-scattering calculations of X-ray absorption spectra. *Phys. Rev. B - Cond. Mat.* ***52***, 2995 - 3009.

Tables

Table 1: Matrices comparing elemental correlations in maps from thin sections (TS) for LM-A and LM-B.

LM-A

	TS Map 1						TS Map 2						TS Map 3						
	As	**Cr**	**Cu**	**Fe**	**Mn**	**Zn**	**As**	**Cr**	**Cu**	**Fe**	**Mn**	**Zn**	**As**	**Cr**	**Cu**	**Fe**	**Mn**	**Zn**	
As		91	35	23	60	88		89	66	44	72	95		87	56	33	50	91	**As**
Cr	91		42	30	68	85	89		66	39	78	91	87		53	33	57	80	**Cr**
Cu	35	42		35	44	57	66	66		48	63	71	56	53		61	61	70	**Cu**
Fe	23	30	35		67	44	44	39	48		57	44	33	33	61		61	55	**Fe**
Mn	60	68	44	67		70	72	78	63	57		76	50	57	61	61		63	**Mn**
Zn	88	85	57	44	70		95	91	71	44	76		91	80	70	55	63		**Zn**

LM-B

	TS Map 1						TS Map 2						TS Map 3						
	As	**Cr**	**Cu**	**Fe**	**Mn**	**Zn**	**As**	**Cr**	**Cu**	**Fe**	**Mn**	**Zn**	**As**	**Cr**	**Cu**	**Fe**	**Mn**	**Zn**	
As		80	63	70	60	93		49	96	27	28	78		75	71	15	28	72	**As**
Cr	80		63	58	58	76	49		43	65	55	55	75		55	13	32	55	**Cr**
Cu	63	63		55	52	68	96	43		24	24	73	71	55		16	23	54	**Cu**
Fe	70	58	55		67	68	27	65	24		78	39	15	13	16		16	14	**Fe**
Mn	60	58	52	67		59	28	55	24	78		36	28	32	23	16		22	**Mn**
Zn	93	76	68	68	59		78	55	73	39	36		72	55	54	14	22		**Zn**

Table 2. XAS reference phase preparation and nomenclature

Reference	pH	Sorbent	mM As (V)	mM Cr/Cu/Zn	# incr.	Γ [μmol g^{-1}] As/Cr/Cu/Zn
Solutions						
Na_2HAsO_4 (aq.)	7.00	0.01M NaCl	25	0/0/0	1	25mM
H_3AsO_3 (aq.)	7.00	0.01M NaCl	25	0/0/0	1	25mM
Sorption Samples						
Goe-4.0a	4.0	Goethite	0.25	0	1	1.41
Goe-4.1	4.0	Goethite	0.25	0/0/0.25	1	1.43
Goe-4.2	4.0	Goethite	2.5	0/0/2.5	1	4.16
Goe-7.0	7.0	Goethite	0.50	0/0/0	1	1.05
Goe-7.1	7.0	Goethite	0.25	0/0/0.25	1	1.08
Goe-7.2	7.0	Goethite	0.25	0/0/0.25	3	3.77
Goe-7.3	7.0	Goethite	0.25	0/0/0.25	6	7.80
Goe-7.4	7.0	Goethite	0.25	0/0/0.25	10	13.20
Goe-7.5	7.0	Goethite	0.50	0/0/0.50	1	1.05
Goe-7.6	7.0	Goethite	0.25	0/0/0.25	2	2.13
Goe-7.7	7.0	Goethite	0.25	0/0.25/0	3	
Goe-7.8	7.0	Goethite	0.25	0/0.25/0.25	3	
Gib-7.0b	7.0	Gibbsite	0.50	0/0/0	1	
Gib-7.1	7.0	Gibbsite	0.25	0/0/0.25	2	
Gib-7.2	7.0	Gibbsite	0.25	0/0/0.25	3	
Gib-7.3	7.0	Gibbsite	0.25	0/0.25/0	3	
Gib-7.4	7.0	Gibbsite	0.25	0/0.25/0.25	3	
Homogeneous Precipitates[c]						
HCAP	7.00	0.01M NaCl	10	0/10/0	1	
HZAP	7.00	0.01M NaCl	10	0/0/10	1	
HCrCAP	7.00	0.01M NaCl	10	10/10/0	1	
HCrZAP	7.00	0.01M NaCl	10	10/0/10	1	
HCZAP	7.00	0.01M NaCl	10	0/10/10	1	
HCrCZAP	7.00	0.01M NaCl	10	10/10/10	1	
Minerals						
Adamite	$Zn_2(AsO_4)OH$					
Allactite	$Mn_7(AsO_4)_4(OH)_2$					
Chalcophyllite	$Cu_9Al(AsO_4)_2(SO_4)_{1.5}(OH)_{12} \cdot 18H_2O$					
Mansfieldite	$AlAsO_4 \cdot 2H_2O$					
Olivenite	$Cu_2(AsO_4)OH$					
Ojuelaite	$ZnFe^{3+}{}_2(AsO_4)_2(OH)_2 \cdot 4\ H_2O$					
Scorodite	$FeAsO_4 \cdot 2H_2O$					
Orpiment	As_2S_3					

(a) Goe = goethite, 4, 7 = pH

(b) Gib = gibbsite, 7 = pH

(c) H = homogeneous, Cr = chromium, C = copper, Z = zinc, A = arsenate, and P = precipitate, e.g., HCrCZAP = homogeneous (mixed) chromic-, copper-, zinc-arsenate precipitate.

Table 3. Summary of structural parameters of EXAFS reference spectra. Only spectra relevant to the PCA/TT and LLSF analyses are displayed.

Reference	As – Ligand				As – Metal				ΔE_0[a]	Res.[b]
	Atom	CN[c] ± 20%	R[d] ± 0.02	σ^{2e}	Atom	CN[c] ± 30%	R[d] ± 0.05	σ^{2e}	eV	
Na_2HAsO_4 (aq.)	O	4.7	1.69	0.0034					3.43	12.88
	O-O-As[f]	9.4	3.10	0.0034						
Sorption Samples										
Goe-4.1	O	5.5	1.70	0.0034	Fe/Zn	1.3	3.30	0.0058	3.61	20.99
	O-O-As	12.0[g]	3.13	0.0034						
Goe-4.2	O	5.1	1.70	0.0027	Fe/Zn	1.3	3.29	0.0045	3.44	11.69
	O-O-As	12.0[g]	3.13	0.0027						
Goe-7.0	O	5.0	1.69	0.0035	Fe	1.6	3.29	0.0061	3.57	30.22
	O-O-As	12.0[g]	3.15	0.0035						
Goe-7.1	O	5.1	1.70	0.0022	Fe/Zn	2.7	3.32	0.0077	3.68	18.86
	O-O-As	12.0[g]	3.19	0.0022	Zn	1.6	3.56	0.0077		
Goe-7.2	O	5.3	1.70	0.0027	Fe/Zn	1.8	3.33	0.0075	3.83	14.05
	O-O-As	12.0[g]	3.12	0.0027	Zn	0.4	3.57	0.0075		
Goe-7.3	O	5.1	1.70	0.0030	Fe/Zn	1.8	3.30	0.0058[£]	3.90	13.32
	O-O-As	12.0[g]	3.16	0.0030	Zn	1.6	3.41	0.0058[£]		
Goe-7.4	O	4.9	1.69	0.0023	Zn	7.8	3.36	0.0110	4.03	10.89
	O-O-As	11.1	3.15	0.0023	Zn-O-As	11.0	3.48	0.0023		
Goe-7.8	O	5.0	1.69	0.0029	Cu	1.4	3.15	0.0060	2.92	15.89
	O-O-As	12.0[g]	3.17	0.0029	Zn/Fe	1.9	3.30	0.0060		
Gib-7.0	O	4.6	1.69	0.0025	Al	1.3	3.16	0.004	4.23	16.66
	O-O-As	12.0[g]	3.05	0.0025						
Gib-7.3	O	5.0	1.69	0.0029	Cu	0.7	3.25	0.0048	3.74	13.26
	O-O-As	13.4	3.00	0.0029	(Al	1.6	3.09)			
Gib-7.4	O	4.9	1.69	0.0024	Al/ Cu	1.4	3.13	0.0060	3.19	11.87
	O-O-As	12.00[g]	3.17	0.0024	Zn/Cu	1.7	3.28	0.0060		
Precipitates & Mineral Phases										
HCZAP	O	4.0	1.69	0.0021	Cu	2.9	3.21	0.0071	2.34	12.35
	O-O-As	n/d			Zn	1.5	3.36	0.0071		
HCAP	O	4.1	1.69	0.0030	Cu	5.2	3.22	0.0085	4.89	18.97
	O-O-As	10.2	3.15	0.0030						
HZAP	O	3.8	1.70	0.0026	Zn	1.0	3.29	0.001	3.77	11.60
	O-O-As	11.8	3.14	0.0026	Zn	1.2	3.43	0.001		
HCrCZAP	O	4.4	1.69	0.0026	Cu	3.9	3.20	0.0092	2.98	16.30
	O-O-As	n/d			Zn	1.2	3.37	0.0092		
HCrCAP	O	4.6	1.69	0.0032	Cu/Cr	6.1	3.21	0.0009	5.80	18.87
	O-O-As	8.6	3.16	0.0032						
HCrZAP	O	4.0	1.69	0.0025	Zn/Cr	3.1	3.36	0.0111	4.24	12.20
	O-O-As	10.9	3.13	0.0025						
Adamite	O	4.5	1.70	0.0023	Zn	7.3	3.35	0.0068	4.29	10.16
	O-O-As	13.5	3.15	0.0023	Zn-O-As	17.7	3.54	0.0023		
Allactite	O	4.6	1.70	0.0022	Mn	2.3	3.11	0.0110	2.81	22.48
	O-O-As	12.0[c]	3.21	0.0022	Mn	3.3	3.45	0.0110		
Chalcophyllite	O	5.3	1.69	0.0034	Cu	5.6	3.34	0.0077	6.84	11.46
	O-O-As	n/d								
Mansfieldite	O	4.3	1.69	0.0028	Al	3.6	3.15	0.0097	3.20	16.88
	O-O-As	6.4	2.98	0.0028						
Olivenite	O	4.7	1.67	0.0044	Cu	4.7	3.27	0.0070	5.22	24.08
	O-O-As	12.0[c]	3.13	0.0044						
Ojuelaite	O	4.4	1.71	0.0035	Fe/Zn	2.2	3.37	0.0084	4.18	11.13
	O-O-As	12.5	3.14	0.0035	Fe	1.6	3.61	0.0084		
Scorodite	O	5.1	1.68	0.0032	Fe	3.6	3.34	0.0049	3.11	24.12
	O-O-As	11.5	3.02	0.0032						

(a) ΔE_0 = phase shift [~eV]
(b) Res. = residual
(c) CN = coordination number
(d) R = radial distance [~Å]

(e) σ^2 = Mean-square relative displacement [~Å^2]: values of the O-O-As MS paths are correlated to the As-O path. For fits with more than one second shell, the second shell σ^2 values are correlated to each other.
(f) O-O-As represents multiple scattering (MS) in the As tetrahedron with an ideal CN of 12, Zn-O-As represents MS between As and Zn with an ideal CN of 16 in adamite.
(g) fixed parameter.

Table 4. Oxidation State Analysis of soil spectra in LM-A and LM-B.

	Letter in Fig. 4		AsO_4 +5	AsO_3 +3	As_2S_3 +3	Total	SS[a]	SS-Abs[b]
LM-A (n = 8)								
Sand ZnAsSpot	A		0.97	0.10	0.00	1.07	0.0037	0.0546
SSCMIX[c] AsMnSpot	B		0.99	0.00	0.06	1.05	0.0017	0.0330
SiCl[d]	C		0.99	0.00	0.04	1.03	0.0022	0.0430
Average (n = 8)[e]			**0.999**	**0.013**	**0.013**	**1.024**	**0.009**	**0.069**
STDV[e]		**±**	**0.018**	**0.033**	**0.022**	**0.026**	**0.011**	**0.053**
LM-B (n = 11)								
Map A Spot 1	D		0.92	0.17	0.10	1.19	0.0174	0.1240
Map B Spot 1	E		0.79	0.23	0.00	1.02	0.0586	0.2290
Sand Map 3 Spot 1	F		0.94	0.18	0.00	1.12	0.0149	0.1070
Average (n = 11)[e]			**0.932**	**0.053**	**0.009**	**0.994**	**0.016**	**0.105**
STDV[e]		**±**	**0.068**	**0.087**	**0.029**	**0.094**	**0.015**	**0.049**

(a) SS = sum-square = $\Sigma((y-y_{fit})^2)/\Sigma(y^2)$

(b) SS-Abs = sum-square absolute = $\Sigma(|y-y_{fit}|)/\Sigma(|y|)$

(c) SSCMIX = sand silt clay mixture

(d) SiCl = silt clay mixture only

(e) Average and standard deviation (STDV) are calculated based on 8 and 11 spectra for LM-A and LM-B, respectively. The missing spectra did not have contributions from AsO_3 or As_2S_3.

Table 5a. Principal component analysis for unknown soil spectra from LM-A and LM-B.

PC#[a]	Eigenvalue	% marginal D Eigenvalue[b]	IND[c]	NSS (tot.)[d]	% marginal D NSS (tot.)[e]
				1	
0	319	-	0.0179	0.0513	0.9487
1	39.8	0.8752	0.0165	0.0365	0.2885
2	28.8	0.2764	0.0161	0.0287	0.2140
3	24.2	0.1597	0.0160	0.0233	0.1882
4	22.1	0.0868	0.0159	0.0187	0.1974
5	18.6	0.1584[f]	0.0160	0.0155	0.1711
6	16.0	0.1398	0.0165	0.0131	0.1548
7	15.3	0.0438	0.0169	0.0109	0.1680
8	12.8	0.1634	0.0177	0.00939	0.1385
9	12.3	0.0391	0.0186	0.00798	0.1502
10	11.5	0.0650	0.0196	0.00675	0.1541

(a) PC# = principal component number
(b) % marginal Δ Eigenvalue $=[(\text{eigenv.})_i-(\text{eigenv.})_{ii}]/(\text{eigenv.})_i$
(c) IND = Malinowski indicator value
(d) NSS (tot.) = normalized sum-square total
(e) % marginal Δ NSS (tot.) $=[(\text{eigenv.})_i-(\text{eigenv.})_{ii}]/(\text{eigenv.})_i$
(f) grey shaded numbers denote a break in an increasing or decreasing number series

Table 5b. Target transformation analysis and SPOIL values from computations with four principal components.

Letter	**SPOIL**[a]	**Reference**
A	1.71	Goe-7.2
B	1.74	HCrCAP
C	1.94	Scorodite
D	2.00	Goe-7.4
E	2.01	HCZAP
F	2.15	Adamite
G	2.20	Gib-7.3
H	2.28	Goe-4.2
I	2.29	Goe-7.8
J	2.33	HCrCZAP
K	2.40	Chalcophyllite
L	2.40	Goe-7.3
M	2.43	Gib-7.4
N	2.51	Ojuelaite
O	2.53	Goe-4.1
P	2.57	Goe-7.1
Q	2.60	Mansfieldite
R	2.63	HZAP
S	2.69	HCrZAP
T	2.81	Goe-7.7

(a) $\text{SPOIL} = [[N(M-C)\Sigma_i(\check{a}_i^{ref}-a_i^{ref})^2]/[(N-C)\Sigma^M_{\alpha=C+1}\lambda_\alpha^2\,\Sigma^C_{\alpha=1}\{\lambda_\alpha^{-1}\,\Sigma_i\,E^\alpha_i\,a_i^{ref}\}^2] - 1]^{1/2}$
For more detail about SPOIL, consult (Malinowski, 1978; Manceau et al., 2002).

Table 6. Linear least-square combination fits for spectra from LM-A and LM-B.

Sample	Component 1		Component 2		Component 3		Fit Statistics		
LM-A	**Name**	**Value**	**Name**	**Value**	**Name**	**Value**	**Total**	**SS[a]**	**SAV[b]**
Map C Spot 1	HCrCZAP	0.72	Scorodite	0.32			1.04	0.0243	0.143
Map C Spot 2	Mansfieldite	0.54	HCrCZAP	0.53			1.07	0.0159	0.115
Map C Spot 3	Goe-7.8	0.95					0.95	0.0261	0.153
Sand AsSpot	Olivenite	0.69	HCAP	0.32	Adamite	0.20	1.01	0.0288	0.155
Sand ZnSpot	Goe-7.8	0.83	HCrZAP	0.29			1.12	0.0349	0.148
SSCMIX AsFeSpot	Goe-7.0	0.53	HCrCZAP	0.47			1.00	0.0346	0.149
SSCMIX AsMnSpot	Gib-7.4	0.93					0.93	0.0262	0.134
SICL AsSpot	Gib-7.3	0.67	Chalcophyllite	0.26			0.93	0.0287	0.134
TS Map 2 Spot 1	HCrZAP	0.67	Chalcophyllite	0.33			1.00	0.0346	0.170
TS Map 2 Spot 2	Gib-7.3	0.57	Goe-7.0	0.28			0.85	0.0194	0.0121
TS Map 2 Spot 3	HCZAP	0.82					0.82	0.0518	0.209
TS Map 3 Spot 1	Gib-7.3	0.82	Chalcophyllite	0.11			0.93	0.0158	0.115
TS Map 3 Spot 2	Goe-7.7	0.48	Gib-7.0	0.43			0.91	0.0265	0.140
Average		***0.71***		***0.25***		***0.02***	***0.98***	***0.0283***	***0.137***
LM-B									
Map 1 Spot 1	HCrCAP	1.15					1.15	0.0870	0.254
Map A AsSpot	HCrCZAP	0.64	Goe-7.2	0.36			1.00	0.0151	0.107
Map B AsSpot	HCuZnAsP.	1.03					1.03	0.0561	0.215
Sand Spot 1	Goe-4.1	0.72	Allactite	0.18			0.90	0.0330	0.153
Sand Spot 2	Gib-7.3	0.93					0.93	0.0389	0.162
Sand Spot 3	Gib-7.3	0.87					0.87	0.0839	0.250
SSCMIX Map 1 AsSpot	Gib-7.4	0.86					0.86	0.0763	0.213
SSCMIX Map 2 N-Spot	Goe-7.8	0.84					0.84	0.0573	0.198
SSCMIX Map 2 C-Spot	Gib-7.1	0.52	HCrCZAP	0.41			0.93	0.0428	0.155
SSXMIX Map 2 S-Spot	Gib-7.1	0.88					0.88	0.104	0.237
SICL AsSpot	Gib7.3	0.93					0.93	0.0685	0.200
TS Map 1AsDiffuseSpot	Goe-7.8	0.86					0.86	0.0293	0.159
TS Map 1 AsHotspot	Mansfieldite	0.67	HCrCZAP	0.37			1.04	0.0168	0.118
TS Map 2 Spot 1	HCrCAP	0.95	Allactite	0.17			1.12	0.0122	0.0908
TS Map 2 Spot 2	Gib-7.3	0.78	Chalcophyllite	0.20			0.98	0.0196	0.107
TS Map 2 Spot 3	HCrCAP	0.80	Gib-7.1	0.28			1.08	0.0102	0.090
Average		***0.84***		***0.12***			***0.96***	***0.0469***	***0.169***

SS = sum-square $= \Sigma((y-y_{fit})^2)/\Sigma(y^2)$ SAV = Sum-absolute value $= \Sigma(|y-y_{fit}|)/\Sigma(|y|)$

Figure Captions

Fig. 1. Soil characterization of LM-A and LM-B. Bulk elemental concentrations were determined from total HNO_3 acid digests.

Fig. 2. Replenishment desorption study for LM-A and LM-B. With increasing strength of the desorbing agent, more As, Cr, Cu, and Zn are released. Zinc appeared to be more labile than the other metals, which suggests that it may have had a different (shorter) residence time.

Fig. 3.: Matrices of Pearson correlations between elements within micro-fluorescence maps.

Fig. 4a. LM-A Map C (powder-on-tape). Map 4A is a CuZnAs micro-fluorescence map of ~ 1x1 mm size and 5x5 μm (HxV) pixel size. Numbers 1-3 show the three spots on which μ-EXAFS data were collected. Maps a-c show the ~ 65 μm diameter spot 2 in the dashed box in map 4A. The micro-fluorescence maps show banding of As, Cr, Cu, and Zn around a central Fe hotspot. (4d) shows line profiles along the arrow shown in map a for As, Cr, Cu, Fe, and Zn. The fluorescence signals of Cr and Cu were amplified by 10 and 5 times, respectively. Quantitative analysis is not possible from this data.

Fig. 4b. LM-B TS Map 2. Map A shows a ~ 2x2 mm AsCuZn micro-fluorescence map scanned with a 5x5 μm (HxV) pixel size. Circles with numbers 1-3 show the three spots

on which μ-EXAFS data were collected. The AsZn scatterplot shows two linear segments which were isolated and remapped showing that Mask 1 and Mask 2 describe two different regions on the map with potentially different make-up with respect to As, Cr, Cu, and Zn.

Fig 5. Fourier transform magnitude of the modulus and imaginary phase for three types of As(V) reference phases (A = aqueous, B = adsorbed, and C = mineral) with (A'-C') and without (A-C) the inclusion of a MS (O-O-As) path. Fits including MS do a better job describing the data than fits without MS for all three types of reference phases.

Fig. 6. Oxidation State Analysis. Graphical analysis of the oxidation states in LM-A and LM-B. "0.0" rel. Kev corresponds to 11.867KeV, which is the muffin tin zero potential of the As^0 K-edge. Letters A-F refer to the six spectra detailed in Table 4.

Fig. 7 A-D. Principal component and target transformation analysis of raw $k^3\chi(k)$ sample spectra (2.75 – 10.50 $Å^{-1}$) for LM-A and LM-B. Graph A displays the first six principal components (0-5, Table 3). Graphs B – D show the target transformation results computed from the first four principal components (0-3) displaying the original references (solid lines) and their transforms (dotted lines) ordered according to the magnitude of the SPOIL values (see Table 4).

Fig. 8A. LM-A Map C. LLSF analysis. The lack of structure in the residual of the $k^3\chi(k)$ functions indicated that the selected references and their amounts reproduced the

unknown spectrum well. Corresponding Fourier transforms, displaying both the magnitudes and imaginary portions, are shown to the right. The results suggest the presence of mixed Cu-Zn-As phases.

Fig. 8B. LM-B TS Map 2. LLSF analysis. The lack of structure in the residual of the $k^3*\chi(k)$ functions indicated that the selected references and their amounts reproduced the unknown spectrum well. Corresponding Fourier transforms, displaying both the magnitudes and imaginary portions, are shown to the right. The LLSF results show the dominance of Cu-Cr-As precipitates in this particle.

Fig. 9. Ternary Plot. Summary of LLSF Analysis for LM-A and LM-B.

Figures:

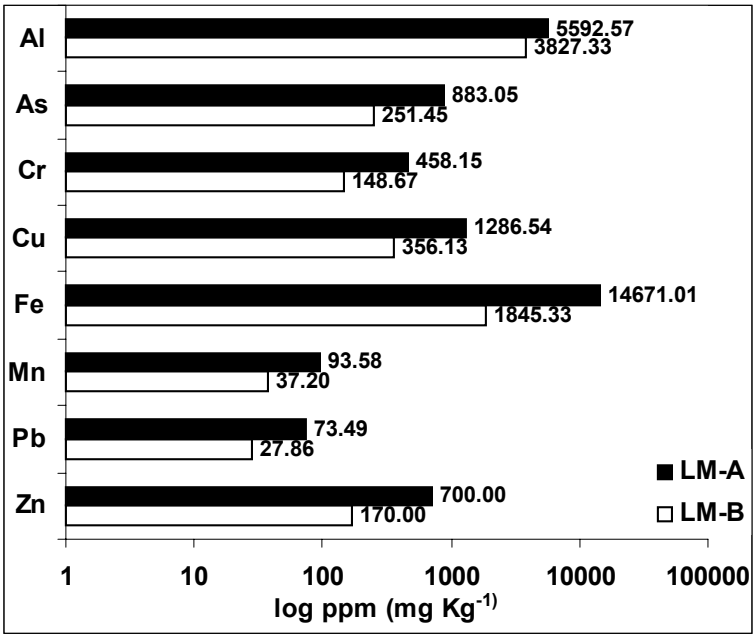

Soil	pH	% Sand[a]	% Silt	% Clay	OM (wt.%)[b]	CEC (pH 7)[c]	CEC (pH 5)[d]	Crystalline Components[e]
LM-A	**7.0-7.5**	**82**	**15**	**3**	**2.9**	**10.06**	**6.67**	**Quartz, kaolinite**
LM-B	**7.0-7.5**	**85**	**14**	**1**	**1.2**	**6.06**	**3.78**	**Quartz, kaolinite**

[a] % sand, silt, and clay fraction determined from hydrometer readings after settling times in 80mM hexa-metaphosphate of 30 sec. and 2 hours.
[b] Determined by loss on ignition.
[c] Mg/Ca exchange at pH 7; units = meq_c $100g^{-1}$ soil.
[d] Acetate exchange at pH 5; units = meq_c $100g^{-1}$ soil.
[e] bulkX-ray diffraction.

Figure 1

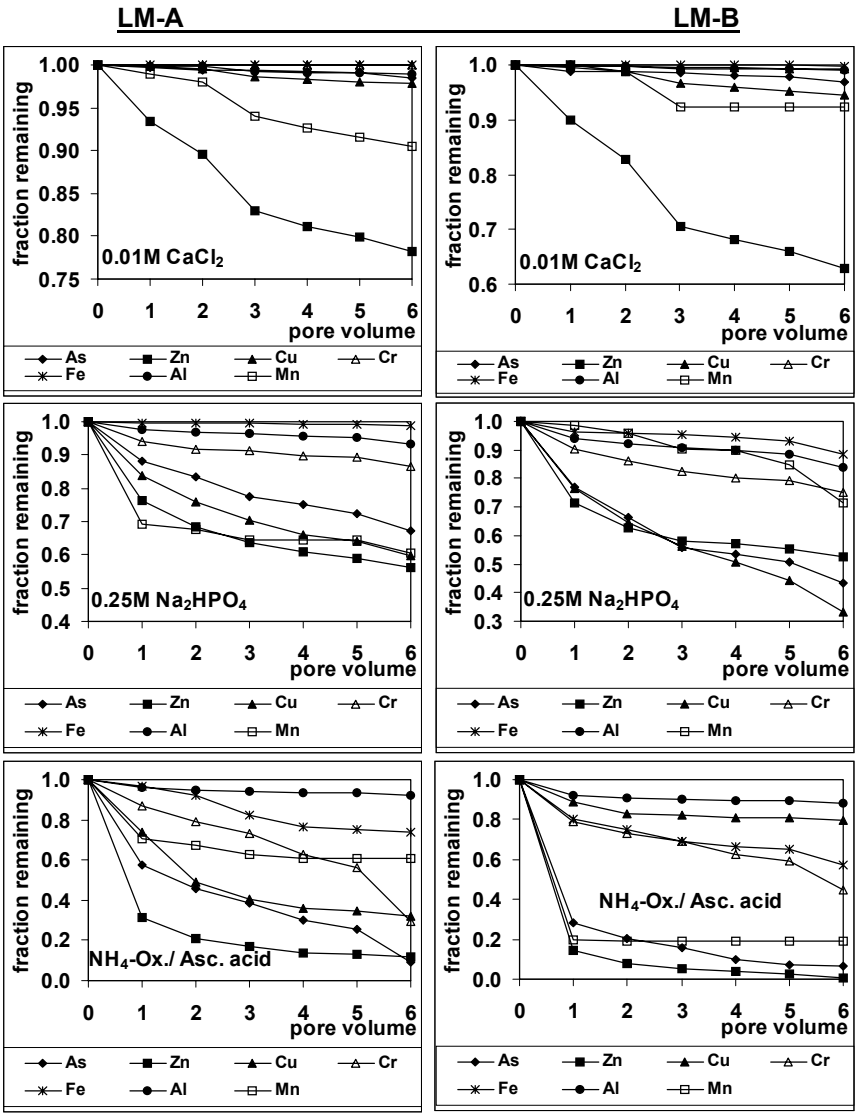
LM-A
LM-B
fraction remaining
pore volume
0.01M CaCl2
0.25M Na2HPO4
NH4-Ox./ Asc. acid
As
Zn
Cu
Cr
Fe
Al
Mn

Figure 2

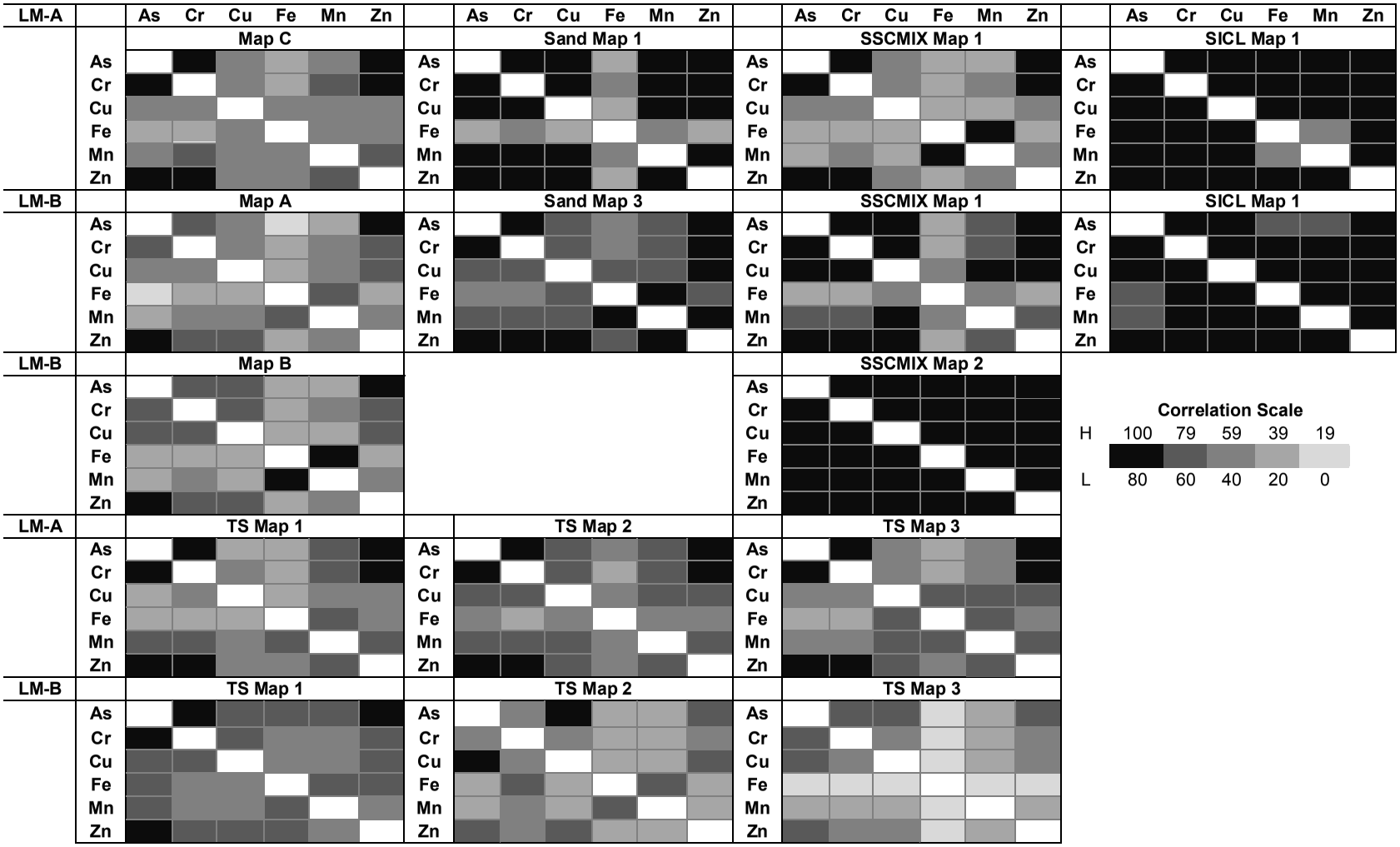
LM-A
Map C
Sand Map 1
SSCMIX Map 1
SICL Map 1
LM-B
Map A
Sand Map 3
SSCMIX Map 1
SICL Map 1
LM-B
Map B
SSCMIX Map 2
LM-A
TS Map 1
TS Map 2
TS Map 3
LM-B
TS Map 1
TS Map 2
TS Map 3
As Cr Cu Fe Mn Zn
Correlation Scale
H 100 79 59 39 19
L 80 60 40 20 0

Figure 3

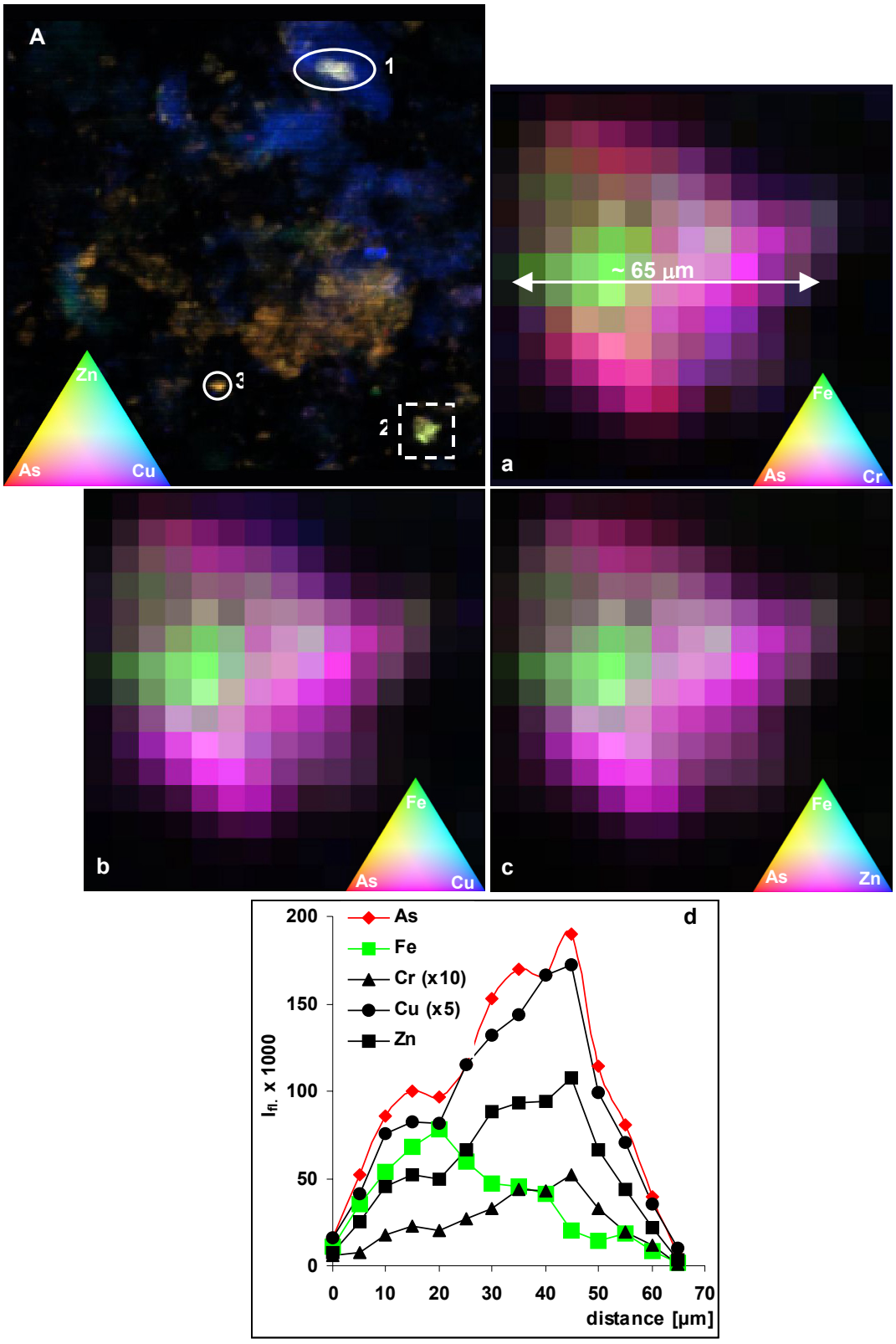
A
1
2
3
Zn
As
Cu
a
~ 65 µm
Fe
As
Cr
b
Fe
As
Cu
c
Fe
As
Zn
d
As
Fe
Cr (x10)
Cu (x5)
Zn
I fl. x 1000
distance [µm]

Figure 4a

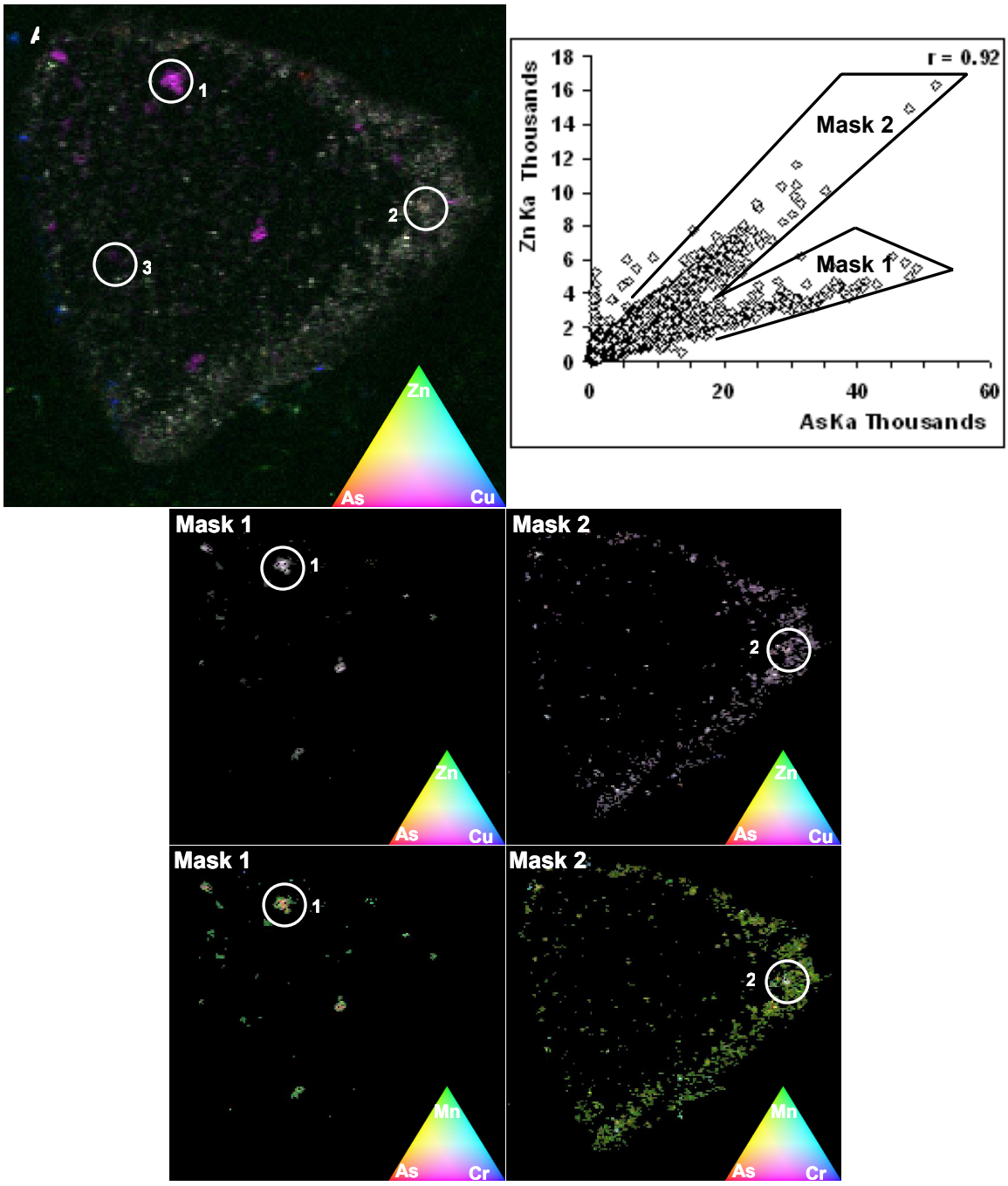
A
1
2
3
Zn
As
Cu
r = 0.92
Mask 2
Mask 1
Zn Ka Thousands
AsKa Thousands
0
2
4
6
8
10
12
14
16
18
0
20
40
60
Mask 1
1
Zn
As
Cu
Mask 2
2
Zn
As
Cu
Mask 1
1
Mn
As
Cr
Mask 2
2
Mn
As
Cr

Figure 4b

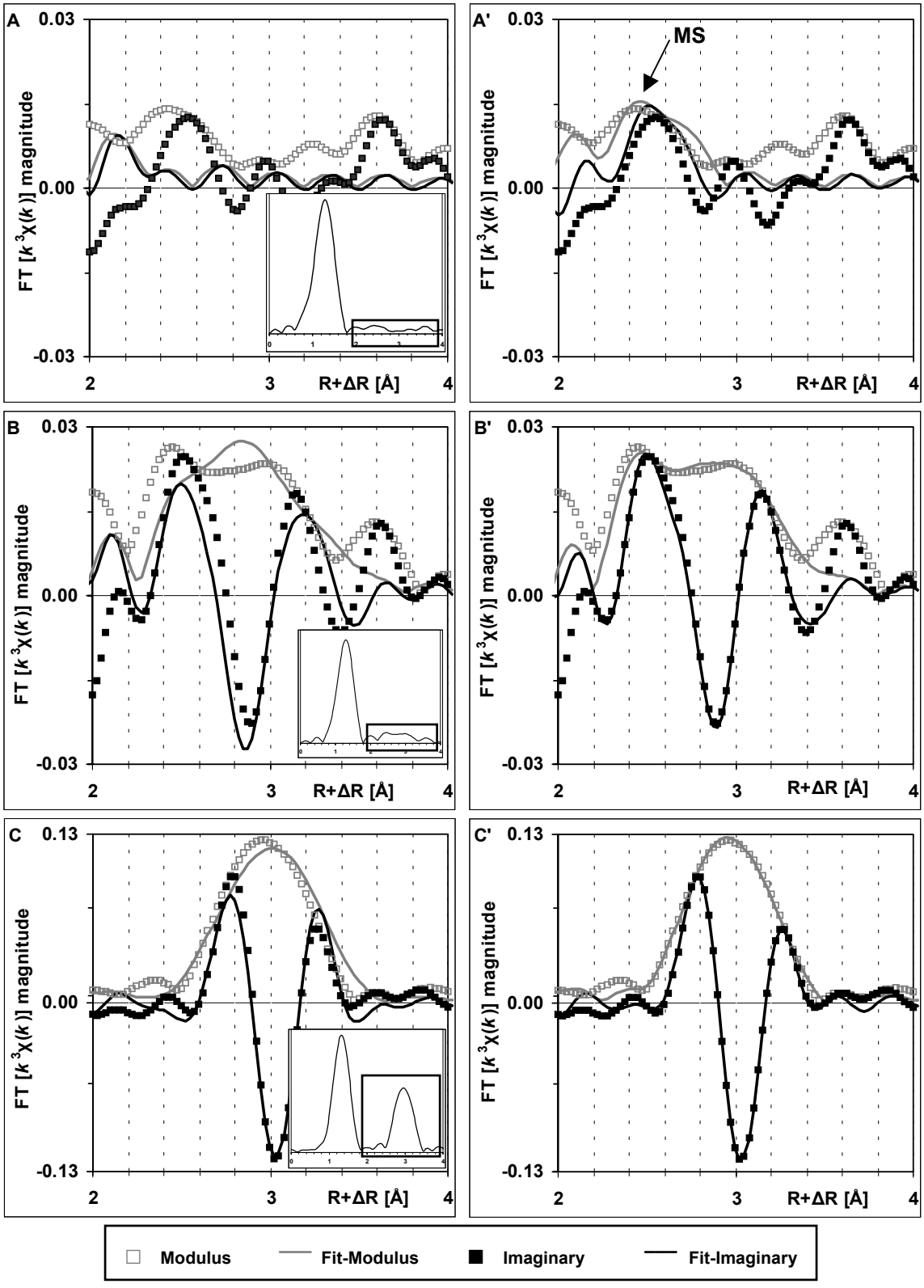
A
A'
B
B'
C
C'
MS
0.03
0.00
-0.03
0.13
-0.13
2
3
4
R+ΔR [Å]
FT [k 3χ(k)] magnitude
Modulus
Fit-Modulus
Imaginary
Fit-Imaginary

Figure 5

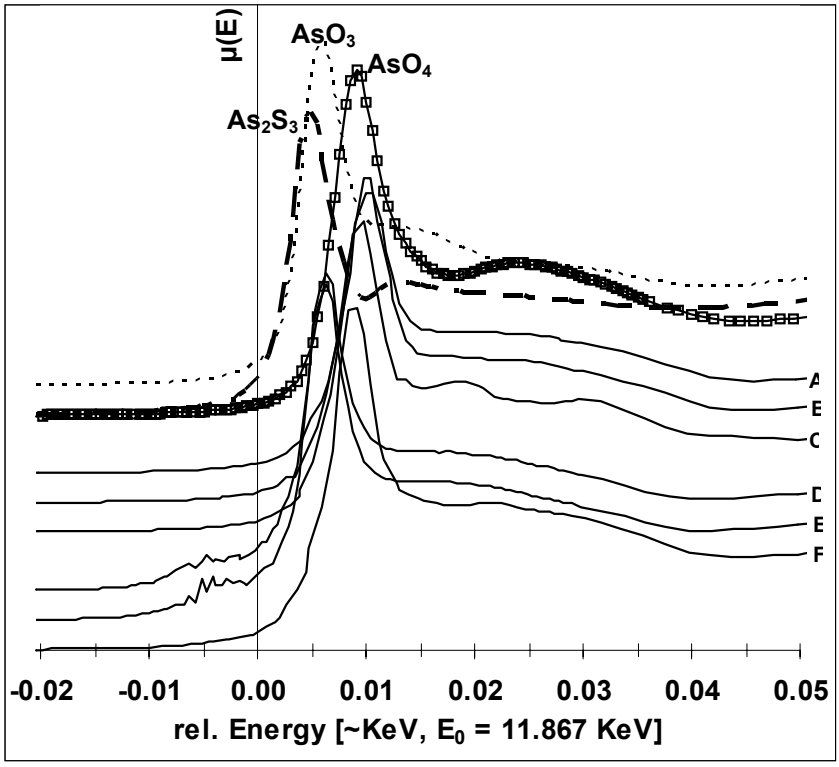
μ(E)
AsO3
AsO4
As2S3
A
B
C
D
E
F
-0.02
-0.01
0.00
0.01
0.02
0.03
0.04
0.05
rel. Energy [~KeV, E0 = 11.867 KeV]

Figure 6

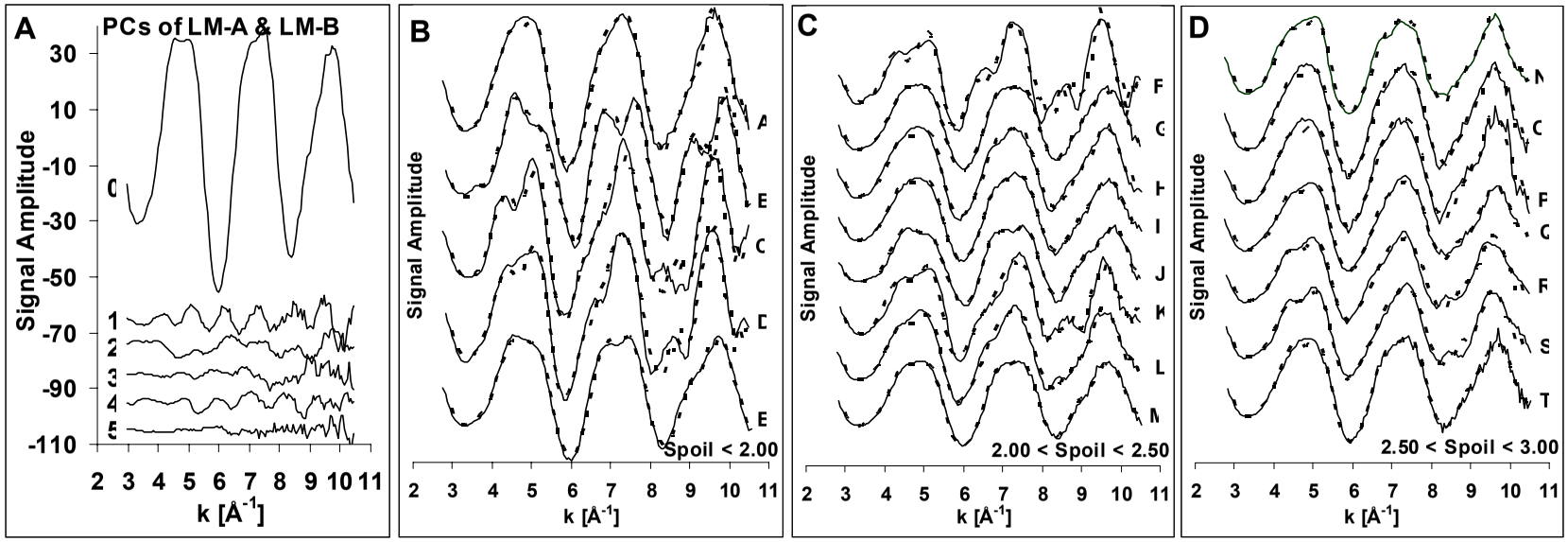
A
PCs of LM-A & LM-B
Signal Amplitude
30
10
-10
-30
-50
-70
-90
-110
2 3 4 5 6 7 8 9 10 11
k [Å-1]
B
Signal Amplitude
Spoil < 2.00
2 3 4 5 6 7 8 9 10 11
k [Å-1]
C
Signal Amplitude
2.00 < Spoil < 2.50
2 3 4 5 6 7 8 9 10 11
k [Å-1]
D
Signal Amplitude
2.50 < Spoil < 3.00
2 3 4 5 6 7 8 9 10 11
k [Å-1]

Figure 7A-D

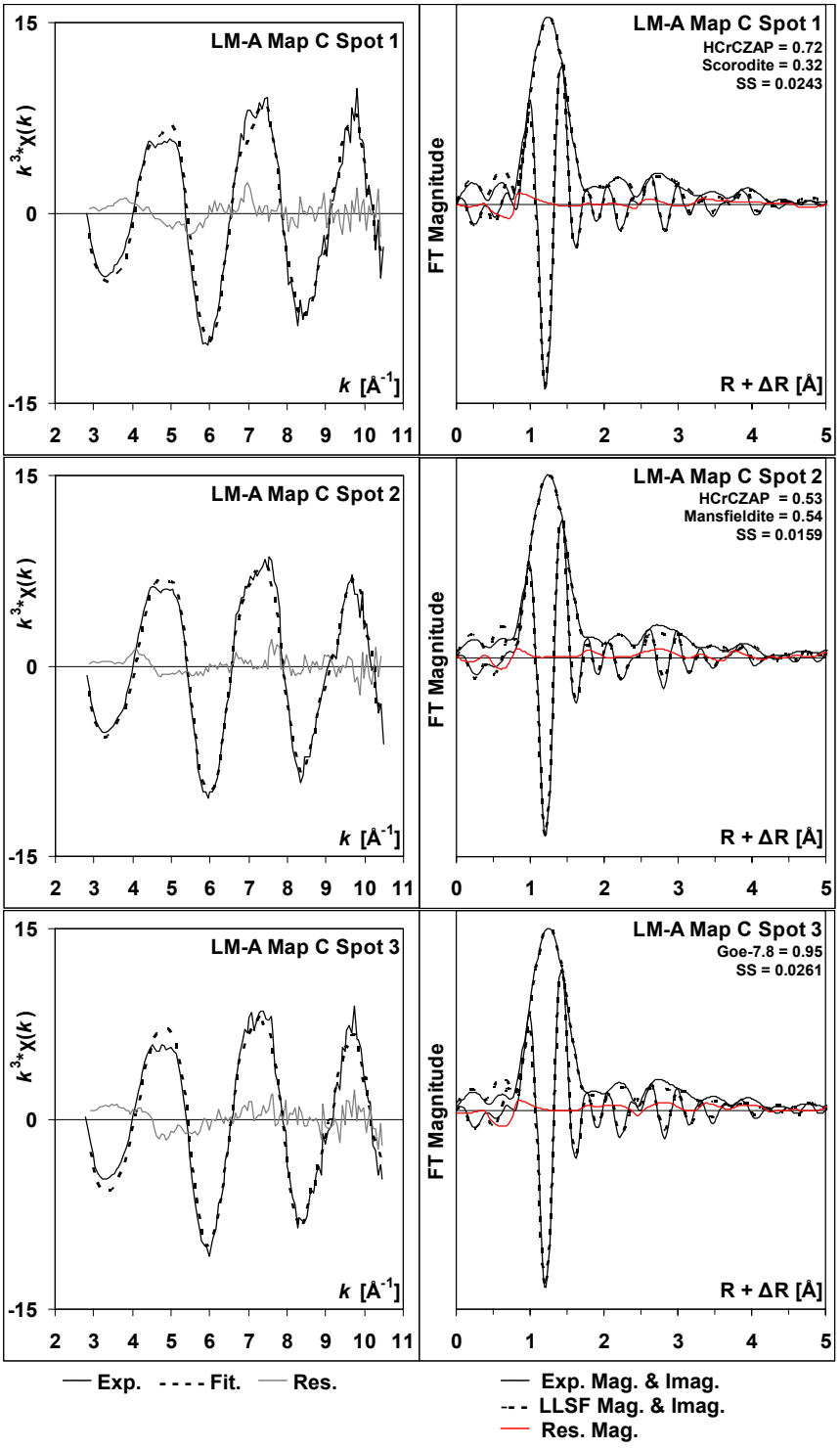
LM-A Map C Spot 1
HCrCZAP = 0.72
Scorodite = 0.32
SS = 0.0243
LM-A Map C Spot 2
HCrCZAP = 0.53
Mansfieldite = 0.54
SS = 0.0159
LM-A Map C Spot 3
Goe-7.8 = 0.95
SS = 0.0261
k³*χ(k)
k [Å⁻¹]
FT Magnitude
R + ΔR [Å]
Exp. - - - - Fit. Res.
Exp. Mag. & Imag.
LLSF Mag. & Imag.
Res. Mag.

Figure 8a

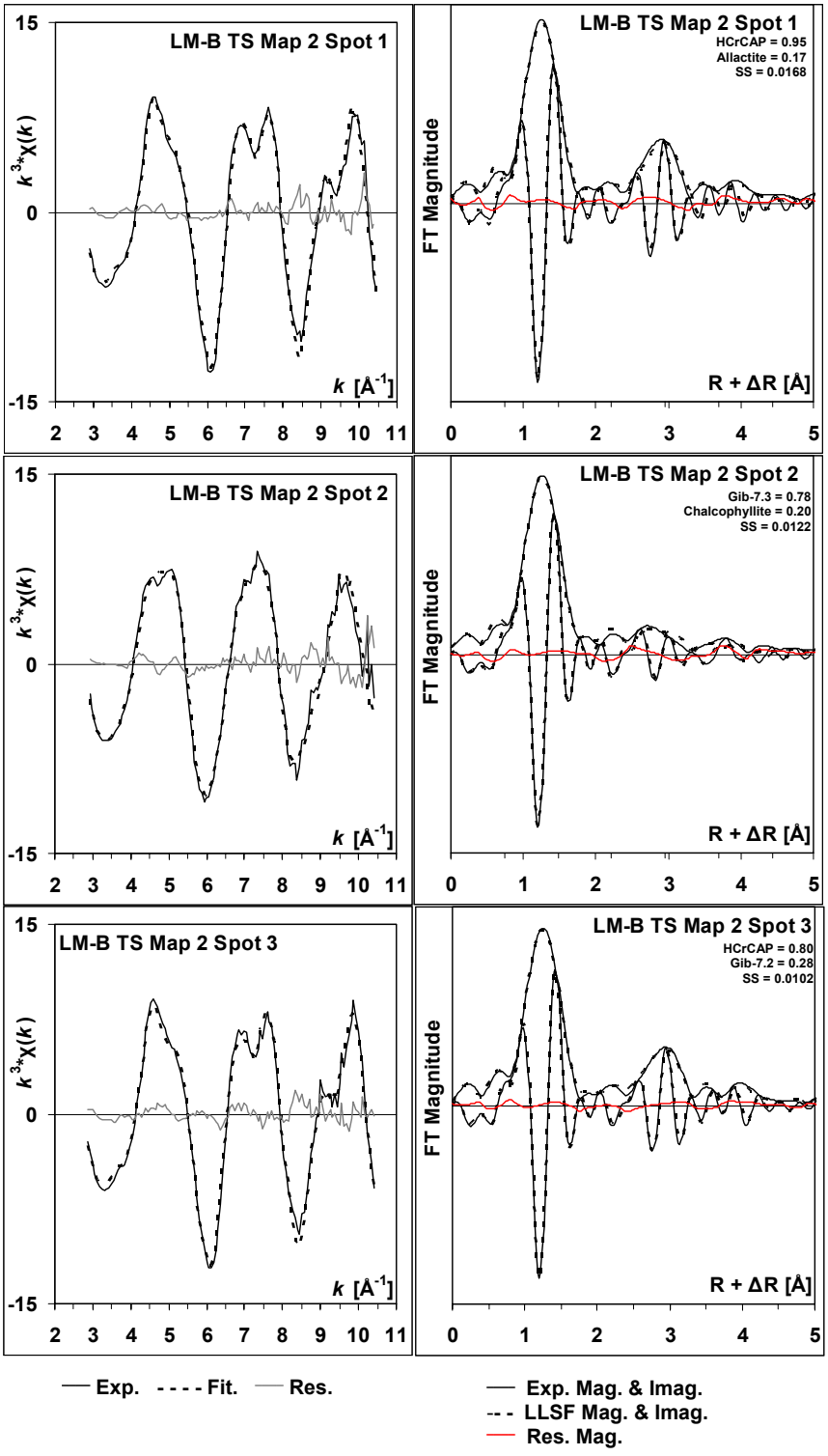
LM-B TS Map 2 Spot 1
LM-B TS Map 2 Spot 1
HCrCAP = 0.95
Allactite = 0.17
SS = 0.0168
LM-B TS Map 2 Spot 2
LM-B TS Map 2 Spot 2
Gib-7.3 = 0.78
Chalcophyllite = 0.20
SS = 0.0122
LM-B TS Map 2 Spot 3
LM-B TS Map 2 Spot 3
HCrCAP = 0.80
Gib-7.2 = 0.28
SS = 0.0102
k³*χ(k)
k [Å⁻¹]
FT Magnitude
R + ΔR [Å]
Exp. Fit. Res.
Exp. Mag. & Imag.
LLSF Mag. & Imag.
Res. Mag.

Figure 8b

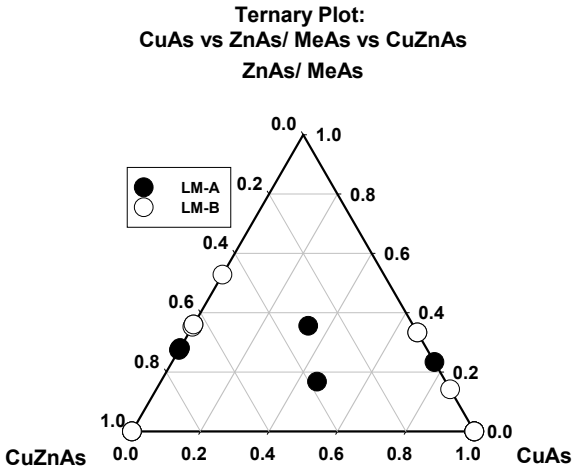

Summary				Ternary Plot Paired t-test[a]		
	LM-A %	LM-B %		T statistic	P	Degrees of freedom
CuAs	33.6	42.3		-0.642	0.549	5
CuZnAs	41.5	32.5		0.302	0.775	5
ZnAs	8.2	17.9		1.162	0.298	5
Al/Fe/Mn-As	16.6	6.6				
Total	99.9	99.3				

(a) The Paired t-test compares contributions from CuAs, CuZnAs, and Zn/Me-As between LM-A and LM-B based on the same set of values used for the ternary plot and determines if the mean values of two data columns are significantly different by testing the hypothesis that the means of the two columns are equal.

Figure 9